Geosci. Model Dev. Discuss., https://doi.org/10.5194/gmd-2019-97
Manuscript under review for journal Geosci. Model Dev.
Discussion started: 14 May 2019

Geoscientific Model Development Discussions

Version 1 of a sea ice module for the physics based, detailed, multi-layer SNOWPACK model

Nander Wever[1,2,3], Leonard Rossmann[4], Nina Maaß[5], Katherine C. Leonard[1,2,6], Lars Kaleschke[4], Marcel Nicolaus[4], and Michael Lehning[2,3]

[1]Department of Atmospheric and Oceanic Sciences, University of Colorado Boulder, Boulder, CO, USA.
[2]CRYOS, School of Architecture, Civil and Environmental Engineering, EPFL, Lausanne, Switzerland.
[3]WSL Institute for Snow and Avalanche Research SLF, Davos, Switzerland.
[4]Alfred Wegener Institute, Helmholtz Centre for Polar and Marine Research, Bremerhaven, Germany.
[5]University of Hamburg, Germany.
[6]Cooperative Institute for Research in Environmental Science (CIRES), University of Colorado Boulder, Boulder, CO, USA.

Correspondence: NANDER WEVER (nander.wever@colorado.edu)

Abstract. Sea ice is an important component of the global climate system. The presence of a snowpack covering sea ice can strongly modify the thermodynamic behaviour of the sea ice, due to the low thermal conductivity and high albedo of snow. The snowpack can be strongly stratified and change properties (density, water content, grain size and shape) throughout the seasons. Fresh water percolation during snow melt can decrease the salinity of the underlying ice, while flooding of the snow layer by saline ocean water can strongly impact both the ice mass balance and the freezing point of the snow. To capture the complex dynamics from the snowpack, we introduce modifications to the physics-based, multi-layer SNOWPACK model to simulate the snow-sea ice system. This involves modifications to the model thermodynamics and to describe water and salt transport through the snow – sea ice system by coupling the transport equation to the Richards equation. These modifications allow the snow microstructure descriptions developed in the SNOWPACK model to be applied to sea ice conditions as well. Here, we drive the model with data from Snow and Ice Mass-balance Buoys installed in the Weddell Sea in Antarctica. The model is able to simulate the temporal evolution of snow density, grain size and shape and snow wetness. The model simulations show abundant depth hoar layers and melt layers, as well as superimposed ice formation due to flooding and percolation. Gravity drainage of dense brine is underestimated as convective processes are so far neglected. Furthermore, with increasing model complexity, detailed forcing data for the simulations is required, which is difficult to acquire due to limited observations in polar regions.

1 Introduction

Sea ice is an important component of the global climate system (Goosse and Fichefet, 1999; Ferrari et al., 2014, e.g.). During the freezing process of ocean water, salt is expelled from the ice and high salinity, dense water is formed. The negative buoyancy of the resulting dense water is an important mechanism driving global ocean circulation (Gordon, 1988, e.g.,). Sea ice also forms the interface between the ocean and the atmosphere for extended periods of time, altering the surface energy balance (Ledley, 1991; Brandt et al., 2005; Perovich et al., 2011, e.g.).

Geosci. Model Dev. Discuss., https://doi.org/10.5194/gmd-2019-97
Manuscript under review for journal Geosci. Model Dev.
Discussion started: 14 May 2019

Geoscientific Model Development Discussions

Antarctic sea ice is largely snow covered (Allison et al., 1993), which has major implications for the energy and mass balance of sea ice (Eicken et al., 1995; Massom et al., 2001). The layer of snow strongly modifies the energy balance both via its high albedo (Grenfell and Perovich, 1984; Brandt et al., 2005; Perovich et al., 2011), and through the thermal conductivity of snow, which insulates the sea ice and limits ice growth (Maykut and Untersteiner, 1971; Sturm et al., 2002). The thermal conductivity of snow also varies widely based on the snow microstructural properties, indicating the need to explicitly consider those properties (Calonne et al., 2011; Sturm et al., 2002).

Although the effect of snow on the energy balance reduces sea ice growth, it can also provide a positive contribution to the mass balance of the sea ice. The flooding of sea ice by ocean water, occurring when the snow cover pushes the sea ice below sea level, is an important mechanism increasing the ice mass over solely thermal growth in Antarctica (Eicken et al., 1994; Jeffries et al., 1997). Snow melt or rain percolating and accumulating on top of the ice may freeze and cause the formation of superimposed ice (Haas et al., 2001; Nicolaus et al., 2003; Obleitner and Lehning, 2004). The spatial and temporal scale of these processes is poorly known due to the uncertainties in knowledge of snow cover distribution and properties.

Assessing snow amounts on sea ice is not straight-forward from atmospheric forcing alone, as the local precipitation is redistributed by wind, and an unknown fraction of precipitation never accumulates over level ice as it is either blown into leads or accumulates in the lee of surface topography (Déry and Tremblay, 2004; Leonard and Maksym, 2011; Trujillo et al., 2016; Liston et al., 2018; Petty et al., 2018). These processes result in snow depth patterns and accumulation patterns that are typically spatially highly variable (Trujillo et al., 2016; Haas et al., 2017). Also, the wind redistribution and smoothing effect of the snow cover modifies the aerodynamic roughness of the sea ice surface, influencing the momentum flux between atmosphere and sea ice (Andreas, 2002; Weiss et al., 2011) and consequently the large-scale movement of sea ice (Tremblay and Mysak, 1997).

Snow stratigraphy over sea ice can also be highly variable in space and time, and exhibit complex microstructural layering (Massom et al., 1998, 2001; Nicolaus et al., 2009). Strong temperature gradients over shallow snow covers can lead to facetting and grain growth, resulting in layers with facetted snow depth hoar crystals (Toyota et al., 2007; Lewis et al., 2011). Often wind slabs, ice layers and melt-freeze crusts during the melt season are observed. As snow on sea ice is typically relatively shallow, the often complex layering is concentrated in shallow layers, increasing the challenge for numerical models to capture the important processes accurately enough.

Water transport processes in the snowpack can have a strong impact on snow microstructure and the salinity distribution in the snow – sea ice system. Surface melt can create downward water percolation, which refreezes lower down in the snowpack as ice layers or forms superimposed ice (Nicolaus et al., 2009). Upward motion of liquid water has also been observed due to capillary forces (Massom et al., 1998, 2001). Capillary wicking can move salt upward, creating a salty slush layer and frost flowers at the ice surface (Rankin et al., 2002; Domine et al., 2004), which may get buried beneath snow after snow fall, impacting the salinity and water content of the lowest snow layers.

A wide range of sea ice models have been developed (Bitz and Lipscomb, 1999; Maksym and Jeffries, 2000; Ukita and Martinson, 2001; Huwald et al., 2005; Griewank and Notz, 2013; Turner and Hunke, 2014, e.g.). Due to the increasing importance attributed to snow on sea ice, many sea ice models include a description of the snow cover in their models (Lecomte et al., 2011; Notz, 2012). The most important factors considered by sea ice models is the albedo and the insulating effect of the

Geosci. Model Dev. Discuss., https://doi.org/10.5194/gmd-2019-97
Manuscript under review for journal Geosci. Model Dev.
Discussion started: 14 May 2019

snow. However, for deriving sea ice thickness and snow depth from satellite remote sensing, brightness temperatures of snow are also required. These depend strongly on snow stratigraphy and snow properties. Several studies used the snow thermodynamics model SNTHERM, either using the internal sea ice module or coupled to a sea ice model (Jordan et al., 1999; Nicolaus et al., 2006; Chung et al., 2010; Fuller et al., 2015) to improve the thermodynamical upper boundary condition for sea ice, and assessing the snow microstructure on sea ice.

Rather than improving the representation of snow in sea ice models, this paper presents a new sea ice module developed for the physics based, detailed, multi-layer snow cover model SNOWPACK. Our motivation is that the SNOWPACK model has a long development history with a focus on accurately representing physical processes in the snow cover. This includes a detailed representation of snow microstructure as well as liquid water flow processes (Bartelt and Lehning, 2002; Lehning et al., 2002a, b; Wever et al., 2015, 2016). The model has previously been successfully applied in Polar regions. For example, for the Greenland Ice Sheet (Steger et al., 2017), it was found to provide accurate simulations of water flow and refreezing processes. An application to the Antarctic Plateau (Groot Zwaaftink et al., 2013) showed good agreement for new snow density and temperature profiles in a drifting snow dominated environment.

2 Methods

The SNOWPACK model has a long development history regarding snow processes. The model calculates the snow energy balance, the resulting temperature distribution, snow settling (densification), liquid water flow and the evolution of snow microstructure. The snow microstructure is described by four parameters: grain size, bond size, sphericity and dendricity. Governing state equations describe the time evolution of these parameters given snow temperature, density, liquid water content (LWC), etc. The full model description is presented in Bartelt and Lehning (2002); Lehning et al. (2002a, b).

The basic model structure of SNOWPACK is congruent with the mushy-layer theory for sea ice (Hunke et al., 2011; Turner and Hunke, 2014). The model is 1-dimensional, with an arbitrary number of vertical layers of arbitrary depth. Typical layer depth, however, is 1-2 cm. Each layers total volume is subdivided into a part consisting of respectively ice, water and air. Henceforth these layers are called "snow" layers. Note that SNOWPACK also considers soil as a category, which is hereafter ignored in the context of sea ice.

The sea ice extension of the model provides modifications to the model code to include the effect of salinity on thermal properties and liquid water flow. Furthermore, ice growth and melt at the bottom of the domain is assessed. Flooding is considered to occur only in one-dimension, and lateral advection of liquid water is ignored (Maksym and Jeffries, 2000).

Below, we detail the modifications of the SNOWPACK model to make it suitable for sea ice simulations. The modifications are implemented in the main version of SNOWPACK, and sea ice specific settings are only needed in the configuration files for the model. The code base of the SNOWPACK model is the same and future developments in other parts of the code will also be directly available for the sea ice version.

Geosci. Model Dev. Discuss., https://doi.org/10.5194/gmd-2019-97
Manuscript under review for journal Geosci. Model Dev.
Discussion started: 14 May 2019

Geoscientific Model Development Discussions

2.1 Heat equation and thermodynamics

SNOWPACK solves the heat equation using finite elements, as described in Bartelt and Lehning (2002), allowing to have a simulated snow surface temperature as well as a temperature at the bottom of the snow column. Each snow layer, called element, has two nodes with the adjacent elements. Several modifications were necessary to take into account the effect of salinity on thermodynamical properties.

First, it is assumed that all salt is concentrated in the liquid water in the brine pockets and that the volumetric ice content is free of salt, such that one can write:

$$S_b = \frac{S}{\theta}. \tag{1}$$

Here, S is the bulk salinity (g kg^{-1}), S_b is the brine salinity (g kg^{-1}) and θ is the volumetric liquid water content (m^3 m^{-3}).

The melting point T_m (K) of each snow element can then be expressed as a function of brine salinity by the commonly used relationship (Assur, 1960):

$$T_\mathrm{m} = -\mu S_b + T_0, \tag{2}$$

where μ is a constant (0.054 K (g kg^{-1})$^{-1}$) and T_0 is the melting point of fresh water (273.15 K).

To solve the heat equation, we assume equilibrium between the element temperature T_e (K) and the brine melting point T_m. When the ice is heating (cooling), brine is supposed to melt (freeze) instantaneously, in order to maintain $T_\mathrm{e} = T_\mathrm{m}$. This is achieved by feeding back the energy associated with the phase change as a source/sink term in the heat equation (see Eq. 3 in Bartelt and Lehning (2002)). Note that the latent heat released (used) when water freezes (melts) increases (decreases) the temperature locally, thus counteracting the temperature change. In turn, the refreezing (melting) ice would impact brine salinity and thereby the melting temperature. These competing processes slow down the convergence in the solver for the heat equation, which can be mitigated by providing an improved estimate of the melting temperature which satisfies: (i) the condition provided by Eq. 1 for the new LWC, (ii) Eq. 2 for the new melting temperature given the new brine salinity, and (iii) the change in ice content for the given deviation of the new element temperature from the melting point, by algebraically solving these three conditions with the three unknowns.

The bottom node of the domain represents the interface between sea ice and ocean and its temperature is prescribed as a Dirichlet boundary condition using the freezing temperature of the ocean water, which is determined by the prescribed ocean salinity. Typically heat is advected in the ocean from below, referred to as the ocean heat flux. We determine the net energy loss or gain at the bottom node, given the prescribed ocean heat flux and the internal heat flux in the lowest sea ice element. This net energy is translated into bottom ice growth or melt.

An uncertainty for ice growth is the ice porosity of the newly formed ice. We apply a similar approach to the one presented in Griewank and Notz (2013), where an ice content threshold is defined. When the lowest element has an ice content below this value, the net energy is used to create a new ice element with a brine salinity equal to ocean salinity (Vancoppenolle et al., 2010). Otherwise, the bottom element grows in length. We set a threshold of 0.99 m^3 m^{-3}, which we also prescribe as the maximum allowed ice content of a single layer. Mass loss is applied by reducing the element length.

Geosci. Model Dev. Discuss., https://doi.org/10.5194/gmd-2019-97
Manuscript under review for journal Geosci. Model Dev.
Discussion started: 14 May 2019

2.2 Brine dynamics

The SNOWPACK model is equipped with two water transport schemes: a simple bucket scheme and a solver for the full Richards equation for transport in porous media (Wever et al., 2014). Below, we will outline how these water transport schemes were modified for sea ice.

A general modification is that the density of liquid water (ρ) is adjusted for salinity as:

$$\rho = \rho_{\mathrm{w}} + \beta S_{\mathrm{b}}, \tag{3}$$

where ρ_{w} is the density of fresh liquid water (1000 kg m^{-3}), β is a salinity coefficient, approximated as 0.824 kg^2 g^{-1} m^{-3} (Massel, 2015, Appendix A).

2.2.1 Bucket Scheme for simple water transport

One of the simplest approaches to simulate liquid water flow through porous media is the so-called bucket scheme, which is also available for the sea ice module in SNOWPACK. The scheme is described in Wever et al. (2014). For sea ice, the bucket scheme has been extended with a simple description of flooding. The pore space of the part of the simulated domain which is located below sea level is filled with liquid water with ocean water salinity S_{o}. The salinity distribution of the sea ice is described by a fixed salinity profile.

The position of the sea level inside the model domain z_{sl} (m) is determined from the isostatic balance:

$$z_{\mathrm{sl}} = \frac{\mathrm{SWE}}{(\rho_{\mathrm{w}} + \beta S_{\mathrm{o}})}, \tag{4}$$

where SWE is the snow water equivalent, defined as the sum over all elements N of the mass of each element j in the model:

$$\mathrm{SWE} = \sum_{j=1}^{N} (\theta_{\mathrm{i},j}\rho_{\mathrm{i}} + \theta_j \rho_j)\, \Delta z_j, \tag{5}$$

where $\theta_{\mathrm{i},j}$ and θ_j is the volumetric content (m^3 m^{-3}) for layer j of ice and water, respectively. ρ_{i} is the density of ice (917 kg m^{-3}) and ρ_j the brine density of layer j (see Eq. 3).

2.2.2 Explicit brine dynamics

As an alternative to the bucket scheme, a solver for the Richards equation coupled to a transport equation can be used. This provides an explicit treatment of brine dynamics. First, the Richards equation solves the liquid water flow in the snow – sea ice system, keeping the salinity constant with time. After each integration of the Richards equation, the advection-diffusion equation is solved for the same time step under the assumption of constant liquid water fluxes. The time step is limited to a maximum of 15 minutes, although stability criteria for both the Richards equation as well as the advection-diffusion equation for salinity may impose additional, stricter, time constraints.

Geosci. Model Dev. Discuss., https://doi.org/10.5194/gmd-2019-97
Manuscript under review for journal Geosci. Model Dev.
Discussion started: 14 May 2019

Geoscientific Model Development Discussions

Richards equation for explicit water transport

The mixed form of the Richards equation reads:

$$\frac{\partial \theta}{\partial t} - \frac{\partial}{\partial z}\left[\frac{\kappa}{\eta}\frac{\partial p}{\partial z}\right] - s = 0, \tag{6}$$

where t is time (s), z is the vertical coordinate (m), κ is the permeability (m^2), η is the viscosity (m s^{-2}) and s is a source/sink term (m^3 m^{-3} s^{-1}). The pressure p can be considered the sum of water potential and gravity potential:

$$p = \rho g h + \rho g z \cos(\gamma) \tag{7}$$

where h is the pressure head (m), g is the gravitational acceleration (m s^{-1}), ρ the density of the flowing liquid (kg m^{-3}) and γ is the slope angle. Note that SNOWPACK can be used in sloped terrain. For completeness of the model description, we keep this term, although for sea ice γ is obviously 0. The permeability κ is replaced by the hydraulic conductivity K, which relates to κ via:

$$K = \kappa \frac{\rho g}{\mu}, \tag{8}$$

where μ is the dynamic viscosity of water (0.001792 kg (m s)$^{-1}$).

A critical assumption in the typical application of the Richards equation is that it is assumed that both g and ρ are constant in time and z, and consequently can be eliminated from the equation. Due to salinity variations in sea ice, variations of density of the flowing liquid can occur and are actually considered the driving mechanism in the temporal and spatial evolution of the salinity of sea ice.

Therefore, we rewrite the Richards equation for sea ice by considering ρ as a function of z and only eliminating g, arriving at:

$$\frac{\partial \theta}{\partial t} - \frac{\partial}{\partial z}\left[\frac{K}{\rho}\frac{\partial}{\partial z}\left(\rho h + \rho z \cos(\gamma)\right)\right] - s = 0, \tag{9}$$

As outlined in Wever et al. (2014), the Richards equation is implemented in SNOWPACK by the discretization proposed by Celia et al. (1990). The backward Euler approximation in time coupled with a simple Picard iteration, as shown in Eq. 14 of Celia et al. (1990), becomes, for Eq. 9:

$$\frac{\theta^{n+1,m+1} - \theta^{n}}{\Delta t} - \frac{\partial}{\partial z}\left(\frac{K^{n+1,m}}{\rho}\frac{\partial \rho h^{n+1,m+1}}{\partial z}\right) - \cos(\gamma)\frac{\partial K^{n+1,m}}{\partial z} - \cos(\gamma)\frac{\partial}{\partial z}\left(\frac{K^{n+1,m} z}{\rho}\frac{\partial \rho}{\partial z}\right) - s = 0, \tag{10}$$

where n and m denote the time and iteration level, respectively. Here, we have used to chain rule to write:

$$\frac{\partial}{\partial z}\left[\frac{K}{\rho}\frac{\partial}{\partial z}(\rho z)\right] = \frac{\partial}{\partial z}\left[K\frac{\partial z}{\partial z}\right] + \frac{\partial}{\partial z}\left[\frac{K}{\rho} z \frac{\partial \rho}{\partial z}\right] = \frac{\partial K}{\partial z} + \frac{\partial}{\partial z}\left[\frac{K}{\rho} z \frac{\partial \rho}{\partial z}\right] \tag{11}$$

The last term on the right hand side expresses the liquid water flow driven by density differences.

Geosci. Model Dev. Discuss., https://doi.org/10.5194/gmd-2019-97
Manuscript under review for journal Geosci. Model Dev.
Discussion started: 14 May 2019

After applying a Taylor expansion to Eq. 15 of Celia et al. (1990), and defining $\delta^m \equiv \rho h^{n+1,m+1} - \rho h^{n+1,m}$, we arrive at:

$$\left(\frac{1}{\Delta t}\frac{C^{n+1,m}}{\rho}\right)\delta^m + \frac{\theta^{n+1,m}-\theta^n}{\Delta t} - \frac{\partial}{\partial z}\left(\frac{K^{n+1,m}}{\rho}\frac{\partial \rho h^{n+1,m+1}}{\partial z}\right) - \cos(\gamma)\frac{\partial K^{n+1,m}}{\partial z} - \cos(\gamma)\frac{\partial}{\partial z}\left(\frac{K^{n+1,m}}{\rho}z\frac{\partial \rho}{\partial z}\right) - s = 0. \tag{12}$$

Finally, Eq. 16 in Celia et al. (1990) becomes:

$$\left(\frac{1}{\Delta t}\frac{C^{n+1,m}}{\rho}\right)\delta^m - \frac{\partial}{\partial z}\left(\frac{K^{n+1,m}}{\rho}\frac{\partial \delta^m}{\partial z}\right) = \frac{\partial}{\partial z}\left(\frac{K^{n+1,m}}{\rho}\frac{\partial \rho h^{n+1,m+1}}{\partial z}\right) + \cos(\gamma)\frac{\partial K^{n+1,m}}{\partial z} + \cos(\gamma)\frac{\partial}{\partial z}\left(\frac{K^{n+1,m}}{\rho}z\frac{\partial \rho}{\partial z}\right) - \frac{\theta^{n+1,m}-\theta^n}{\Delta t} + s \tag{13}$$

After applying the standard finite difference approximation in space, Eq. 16 in Celia et al. (1990) translates into (i denoting the spatial coordinate):

$$\begin{aligned}
&\frac{C_i^{n+1,m}}{\rho_i}\frac{\delta_i^m}{\Delta t} - \frac{1}{(\Delta z)^2}\left[\frac{K_{i+1/2}^{n+1,m}}{\rho_{i+1/2}}\left(\delta_{i+1}^m - \delta_i^m\right) - \frac{K_{i-1/2}^{n+1,m}}{\rho_{i-1/2}}\left(\delta_i^m - \delta_{i-1}^m\right)\right] \\
&= \frac{1}{(\Delta z)^2}\left[\frac{K_{i+1/2}^{n+1,m}}{\rho_{i+1/2}}\left(\rho_{i+1}h_{i+1}^{n+1,m} - \rho_i h_i^{n+1,m}\right) - \frac{K_{i-1/2}^{n+1,m}}{\rho_{i-1/2}}\left(\rho_i h_i^{n+1,m} - \rho_{i-1}h_{i-1}^{n+1,m}\right)\right] \\
&+ \cos(\gamma)\frac{K_{i+1/2}^{n+1,m} - K_{i-1/2}^{n+1,m}}{\Delta z} + \cos(\gamma)\frac{\frac{K_{i+1/2}^{n+1,m}}{\rho_{i+1/2}}z_{i+1/2}\frac{\rho_{i+1}-\rho_i}{\Delta z} - \frac{K_{i-1/2}^{n+1,m}}{\rho_{i-1/2}}z_{i-1/2}\frac{\rho_i-\rho_{i-1}}{\Delta z}}{\Delta z} - \frac{\theta_i^{n+1,m}-\theta_i^n}{\Delta t} + s_i \\
&\equiv \left(R_i^{n+1,m}\right)_{\mathrm{MPFD}}
\end{aligned} \tag{14}$$

The system of equations described by Equation 14 forms a tri-diagonal matrix. As in Wever et al. (2014), the function `DGTSV` from the `LAPACK` library (Anderson et al., 1999) is called to compute the solution. When `LAPACK` is not available, or not selected on compile time, the Thomas algorithm is used as the implemented default alternative, which does not depend on external libraries. However the Thomas algorithm is not the preferred option as in contrast to `DGTSV`, it lacks partial pivoting and may suffer from numerical instabilities.

Salinity

The governing equation in 1-dimension for concentration describes the change in salinity as a combination of a diffusion and advection process:

$$\frac{\partial}{\partial t}(\theta S_\mathrm{b}) - \frac{\partial}{\partial z}\left(D\theta\frac{\partial S_\mathrm{b}}{\partial z}\right) - \frac{\partial}{\partial z}(qS_\mathrm{b}) - s_\mathrm{sb} = 0 \tag{15}$$

Where D is the diffusion coefficient ($\mathrm{m^2\ s^{-1}}$), considered here as a first approximation independent of temperature, taken as 10^{-10} $\mathrm{m^2\ s^{-1}}$ (Poisson and Papaud, 1983). q denotes the liquid water flux ($\mathrm{m\ s^{-1}}$).

Geosci. Model Dev. Discuss., https://doi.org/10.5194/gmd-2019-97
Manuscript under review for journal Geosci. Model Dev.
Discussion started: 14 May 2019

Geoscientific Model Development Discussions

An implicit numerical scheme for Equation 15 becomes in discretized form (n and i again denoting time and spatial level, respectively):

$$\frac{\left(\theta_i^{n+1} S_{\mathrm{b},i}^{n+1} - \theta_i^n S_{\mathrm{b},i}^n\right)}{\Delta t}$$
$$- f\left[\left(\frac{2D_{i+1}^n \theta_{i+1}^{n+1} S_{\mathrm{b},i+1}^{n+1}}{\Delta z_{\mathrm{up}}\left(\Delta z_{\mathrm{up}} + \Delta z_{\mathrm{down}}\right)} - \frac{2D_i^n \theta_i^{n+1} S_{\mathrm{b},i}^{n+1}}{\left(\Delta z_{\mathrm{up}} \Delta z_{\mathrm{down}}\right)} + \frac{2D_{i-1}^n \theta_{i-1}^{n+1} S_{\mathrm{b},i-1}^{n+1}}{\Delta z_{\mathrm{down}}\left(\Delta z_{\mathrm{up}} + \Delta z_{\mathrm{down}}\right)}\right)\right]$$
$$- (1-f)\left[\left(\frac{2D_{i+1}^n \theta_{i+1}^n S_{\mathrm{b},i+1}^n}{\Delta z_{\mathrm{up}}\left(\Delta z_{\mathrm{up}} + \Delta z_{\mathrm{down}}\right)} - \frac{2D_i^n \theta_i^n S_{\mathrm{b},i}^n}{\left(\Delta z_{\mathrm{up}} \Delta z_{\mathrm{down}}\right)} + \frac{2D_{i-1}^n \theta_{i-1}^n S_{\mathrm{b},i-1}^n}{\Delta z_{\mathrm{down}}\left(\Delta z_{\mathrm{up}} + \Delta z_{\mathrm{down}}\right)}\right)\right]$$
$$- f\left[\left(\frac{q_{i+1}^n S_{\mathrm{b},i+1}^{n+1} - q_{i-1}^n S_{\mathrm{b},i-1}^{n+1}}{\left(\Delta z_{\mathrm{up}} + \Delta z_{\mathrm{down}}\right)}\right)\right] - (1-f)\left[\left(\frac{q_{i+1}^n S_{\mathrm{b},i+1}^n - q_{i-1}^n S_{\mathrm{b},i-1}^n}{\left(\Delta z_{\mathrm{up}} + \Delta z_{\mathrm{down}}\right)}\right)\right] - s_{\mathrm{sb}} = 0 \quad (16)$$

Here, taking $f = 1$ results in a fully implicit scheme, whereas taking $f = 0.5$ corresponds to the Crank-Nicolson scheme (Crank and Nicolson, 1996). The equation is solved after every time step for liquid water flow, assuming that the water flux q is constant with time and can be referenced with the time level n. Furthermore, for LWC θ, both θ^n, as well as θ^{n+1} are known from solving Eq. 14. The domain in SNOWPACK is typically nonuniform and the spatial discretizations in Eq. 16 for the nonuniform grid are based on Veldman and Rinzema (1992). The system of equations described by Equation 16 forms a tri-diagonal matrix, similar to and solved in the same way as the equation for liquid water flow (Eq. 14).

SNOWPACK by default uses the Crank-Nicolson scheme. The fully implicit scheme is only first order accurate, whereas the Crank-Nicolson scheme is second order accurate. Both schemes are unconditionally stable and suffer only minimal numerical diffusion for advection. As with many other common schemes, the advection part does not perfectly conserve sharp transitions. The Crank Nicolson scheme is, in spite of being unconditionally stable, prone to spurious oscillations in the solution. To choose adequate time steps, w apply the CFL condition, typically required for stability of an explicit scheme, also for the Crank-Nicolson scheme:

$$q\frac{\Delta t}{\Delta z} \leq 1 \quad (17)$$

Note that if the CFL condition is violated, the time step is reduced and the last time step for the Richards equation is also repeated with the reduced time step.

Boundary Conditions

The boundary conditions for the Richards equation (Eq. 6) are determined by a Neumann boundary condition at the top, consisting of the top water flux from rain, evaporation or condensation and a Dirichlet boundary condition by prescribing the bottom pressure head. The pressure head at the bottom of the sea ice corresponds to the water pressure at that depth, which equals the sea level (Eq. 4).

The boundary conditions for the advection terms of the advection-diffusion equation (Eq. 15) are prescribed as a Neumann boundary condition, with fresh water at the top, and ocean salinity at the bottom. For the diffusion term, we implemented

Geosci. Model Dev. Discuss., https://doi.org/10.5194/gmd-2019-97
Manuscript under review for journal Geosci. Model Dev.
Discussion started: 14 May 2019

Geoscientific Model Development Discussions

no-flux boundary conditions. These are derived by considering the central differences scheme for the diffusion term on a nonuniform grid, determined according to:

$$\frac{\partial^2}{\partial z^2}\left(D\theta S_{\mathrm{b}}\right) \approx \frac{\frac{D_{i+1}\theta_{i+1}S_{\mathrm{b},i+1}-D_i\theta_i S_{\mathrm{b},i}}{z_{\mathrm{up}}} - \frac{D_i\theta_i S_{\mathrm{b},i}-D_{i-1}\theta_{i-1}S_{\mathrm{b},i-1}}{z_{\mathrm{down}}}}{\frac{1}{2}\left(z_{\mathrm{up}}+z_{\mathrm{down}}\right)} \tag{18}$$

A no-flux boundary condition can be achieved by forcing gradients over the boundaries to be 0, such that either the left (upper boundary) or right (lower boundary) term in the numerator of Eq. 18 vanishes.

Hydraulic Properties

For solving the Richards equation and the salinity transport equation, several parameters which depend on the snow and ice microstructure need to be specified. For saturated hydraulic conductivity (K_{sat}), we define elements with a porosity (i.e., $1-\theta_{\mathrm{i}}$) larger than 0.25 as snow, and smaller than 0.25 as ice.

For snow elements, a formulation based on Calonne et al. (2012) is typically used (see Wever et al. (2014)):

$$K_{\mathrm{sat}} = \left(\frac{\rho g}{\mu}\right)\left[3.0\left(\frac{r_{\mathrm{es}}}{1000}\right)^2 \exp\left(-0.013\theta_{\mathrm{i}}\rho_{\mathrm{i}}\right)\right], \tag{19}$$

where r_{es} is the equivalent sphere radius (m). Note that Eq. 14 in Wever et al. (2014) erroneously shows a factor 0.75 (which corresponds to r_{es} being a grain diameter) instead of 3.0.

For sea ice, the saturated hydraulic conductivity (K_{sat}) is based on Golden et al. (2007):

$$K_{\mathrm{sat}} = 3\cdot 10^{-8}\left(\frac{\rho g}{\mu}\right)\left(1-\theta_{\mathrm{i}}\right)^3 \tag{20}$$

In unsaturated conditions, the van Genuchten-Mualem model (Mualem, 1976) is used to relate the hydraulic conductivity in saturated conditions (Eq. 19 and 20) to unsaturated conditions. Furthermore, in unsaturated conditions, the van Genuchten model is used for the water retention curve, which describes the relationship between capillary suction and LWC (van Genuchten, 1980). The coefficients in this parameterization of water retention in snow is based on the work by Yamaguchi et al. (2012) for snow. We extend this parameterization independent of porosity, by absence of any information of water retention in sea ice as a function of salinity and LWC. It has a relatively small impact, as the largest part of the sea ice is below sea level and thus saturated.

3 Data and Simulation Setup

3.1 In-situ Buoys

We apply the sea ice version of SNOWPACK to snow and sea ice properties measured from two pairs of Snow Buoys and one Ice Mass-balance Buoy (IMB) in the Weddell Sea, Antarctica. Snow Buoys are autonomous ice tethered instruments, which measure snow surface changes/accumulation with four ultrasonic sensors 1.5 m above the snow ice interface (Nicolaus et al.,

Geosci. Model Dev. Discuss., https://doi.org/10.5194/gmd-2019-97
Manuscript under review for journal Geosci. Model Dev.
Discussion started: 14 May 2019

Geoscientific Model Development Discussions
Open Access
EGU

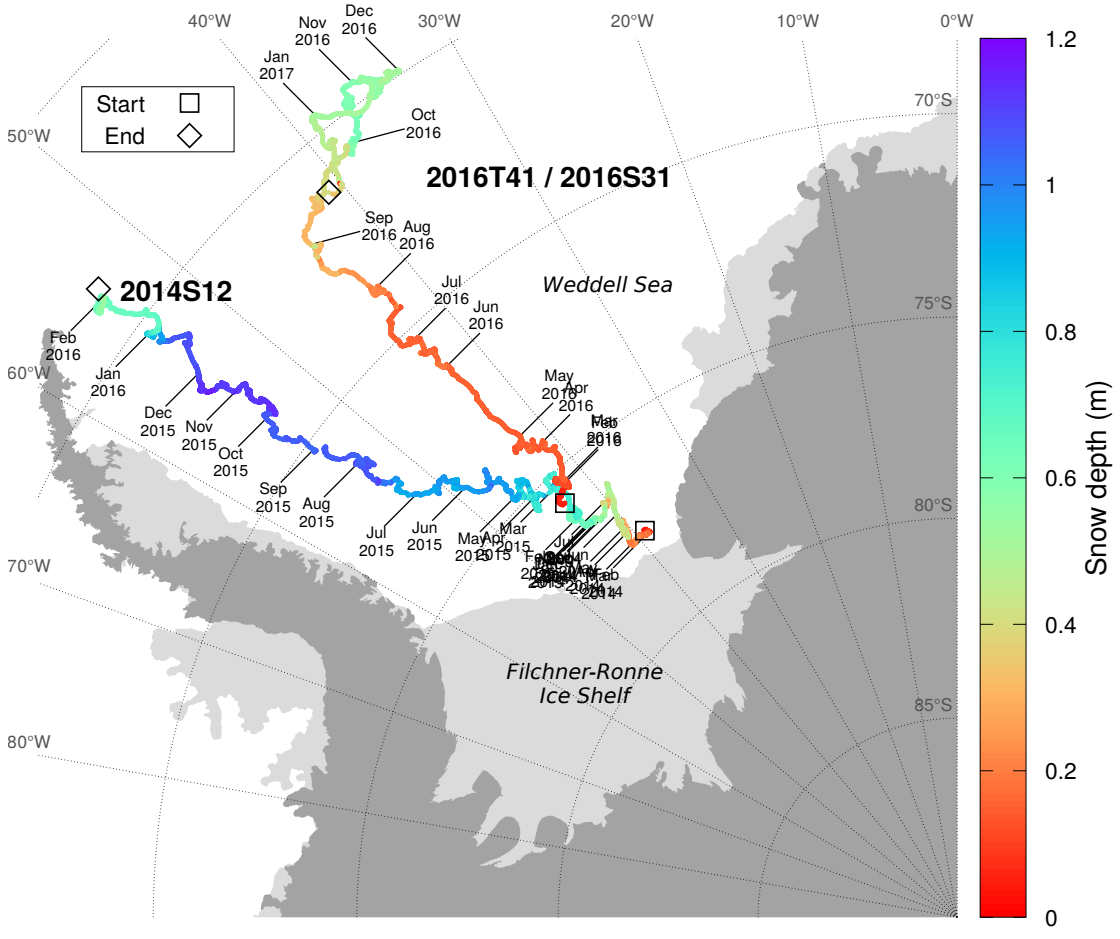

Figure 1. Trajectories of the two sea ice buoys used for the simulations. The average snow depth measured by the four snow depth sensors on each Snow Buoy is shown in color. The location of the buoys on the 1st of each month is labelled by month and year. The collocated IMB buoy for the 2014S12 Snow Buoy (2014T9) stopped transmitting data very soon and is ignored in the analysis. The collocated IMB buoy to Snow Buoy 2016S31 is 2016T41. The deployment location (start) is denoted by a square, the location of the last received data from the buoy (end) is denoted by a diamond.

in prep). We construct a time series by averaging the four snow depth sensors of each buoy. In addition to snow depth, the Snow Buoys measure barometric air pressure and air temperature.

Each IMB consists of a 4.8 m long thermistor string, with a vertical sensor spacing of 0.02 m and provides sea ice temperature as well as interfaces from snow, sea ice, and sea water. The instruments are described by Jackson et al. (2013). It turned out to be good practice to co-deploy Snow Buoys and thermistor string IMBs in order to observe snow depth and sea ice properties at

Geosci. Model Dev. Discuss., https://doi.org/10.5194/gmd-2019-97
Manuscript under review for journal Geosci. Model Dev.
Discussion started: 14 May 2019

the same time. The full data set of all these Lagrangian observations is available from http://www.meereisportal.de (Grosfeld et al., 2015).

The two selected Snow Buoys (Snow Buoys 2014S12 and 2016S31) have long time series and cover different trajectories, as shown in Fig. 1. Unfortunately, IMB 2014T9 collocated with Snow Buoy 2014S12 stopped transmitting data soon after deployment. IMB 2016T41, collocated with Snow Buoy 2016S31 measured for almost the same period as the Snow Buoy. However, comparisons have to focus on the sea ice properties excluding the snow cover on top, because the IMB was deployed directly onto the sea ice surface and the thermistor chain does not measure the snow cover properties, except for the lowest few cm.

Fig. 1 shows the trajectories with labels marking the location at the 1st of each month. Snow Buoy 2014S12 was deployed on 17 Jan 2014 and remained in the same area very close to the Filchner-Ronne Ice Shelf for the first year. From February 2015 onward, the Snow Buoy drifted northward parallel to the Antarctic Peninsula until data transmission was lost on 1 Feb 2016. During the last 18 hours no valid snow depth data were transmitted and the drift speeds were relatively high, suggesting that it is not a transmission or data logger failure, but rather an indication that flow deformation or breakup is the likely cause of the loss of the Snow Buoy. We consider this particular Snow Buoy due to its long time span, even though a collocated IMB data set is not available.

Snow Buoy 2016S31, collocated with IMB Buoy 2016T41, was deployed on 16 Jan 2016. This deployment drifted on a northward course until December 2016. Around the 1st of December, the northernmost position was reached after which the deployment drifted southward again. The Snow Buoy transmitted data up to 15 Jan 2017, 2:00 UTC, shortly before the last data transmission by the IMB Buoy (5 Feb 2017, 07:13 UTC). This combination of Snow Buoy and IMB Buoy is interesting for the long time span of collocated measurements.

3.2 Initial Conditions

To start each simulation, a description of the initial sea ice state is required. Upon installation of each Snow Buoy, the ice thickness, snow thickness and freeboard was determined. For simulations of these Snow Buoys, we distinguish three categories: (i) sea ice below sea level (ice thickness minus freeboard), (ii) sea ice above sea level (freeboard) and (iii) snow.

For the part of the sea ice below sea level, the volumetric ice content θ_i was fixed to 0.9, and the volumetric water content θ_w was subsequently calculated as:

$$\theta_\mathrm{w} = (1 - \theta_\mathrm{i}) \frac{\rho_\mathrm{i}}{\rho_\mathrm{w}} \tag{21}$$

This formulation leaves a small volumetric air content which can be filled when water refreezes and thereby expands. This is currently required for the stability of the numerical schemes in the SNOWPACK model, but in reality refreezing water would increase the pressure in the brine. The element temperature was initialized by the value recorded by the IMB upon installation. As it takes time for the thermistor string to freeze into the ice and adapt to the surrounding ice temperature, this temperature is mostly representative of the ocean water. The brine salinity was set as the salinity for which the melting point corresponds to the measured temperatures.

Geosci. Model Dev. Discuss., https://doi.org/10.5194/gmd-2019-97
Manuscript under review for journal Geosci. Model Dev.
Discussion started: 14 May 2019

For the part of sea ice above sea level, the volumetric ice content θ_i was also fixed to 0.9, but the remaining space was assigned to air content and the bulk salinity was set to 0 g kg^{-1}. Snow was initialized with a density of 275 kg m^{-3}, and a grain size of 0.15 mm. The element temperature was derived from the thermistor string measurements. Finally, the depth of each element was set to 0.02 m.

3.3 Forcing Data

Simulations with the SNOWPACK model require air temperature, relative humidity, incoming shortwave radiation, incoming longwave radiation, wind speed and precipitation. Here, we used ERA5 (European Centre for Medium-range Weather Forecasts ECMFW Reanalysis 5) to provide these parameters to drive the simulations. For each timestep and location, the simulated weather at the closest grid point in the ERA5 model was taken.

SNOWPACK has the possibility to either use a precipitation time series as input to determine when snow fall occurs, or to use a time series of snow depth to interpret increases in measured snow depth as snow fall events when simulated snow depth is below measured snow depth (Lehning et al., 1999). In order to use the latter method for the Snow Buoys and base the mass balance on Snow Buoy data, a layer can be marked in the simulations and tracked throughout the snow – sea ice continuum. By marking the layer that corresponds to the reference level for the snow depth measurements, the measured snow depth can be tracked relative to this marked layer. The output routines of the model have been adapted accordingly to reference the output to either the sea level, or to the marked reference layer.

The ocean heat flux determines the ice mass balance at the bottom of the ice. Its value can be highly variable and dependent on ocean conditions below the sea ice (Ackley et al., 2015). From that study, we use a value of 8 W m^{-2}, unless otherwise noted.

4 Results

4.1 Explicit Brine Dynamics Example

Fig. 2 shows an example of model behaviour when an initially dry and fresh ice layer with a thickness of 1.58 m, consisting of 94% ice and 6% air expressed as volumetric content, is positioned in ocean water with a salinity of 35 g kg^{-1}. The positive pressure head at the bottom of the sea ice corresponds with the pressure exerted by the displaced water. As a consequence, saline water enters the ice matrix (Fig. 2a,c), until it is in equilibrium with the sea level. As the pressure difference of the liquid water inside the ice matrix and the surrounding ocean water is decreasing, the salt influx rate decreases over time (Fig. 2e). The brine salinity corresponds to the brine salinity of ocean water (35 g kg^{-1}, see Fig. 2d), corresponding to a bulk salinity of 1.65 g kg^{-1} (see Fig. 2c). The added mass to the sea ice (Fig. 2b) causes the ice to sink deeper inside the ocean water, decreasing the freeboard (Fig. 2f).

Geosci. Model Dev. Discuss., https://doi.org/10.5194/gmd-2019-97
Manuscript under review for journal Geosci. Model Dev.
Discussion started: 14 May 2019

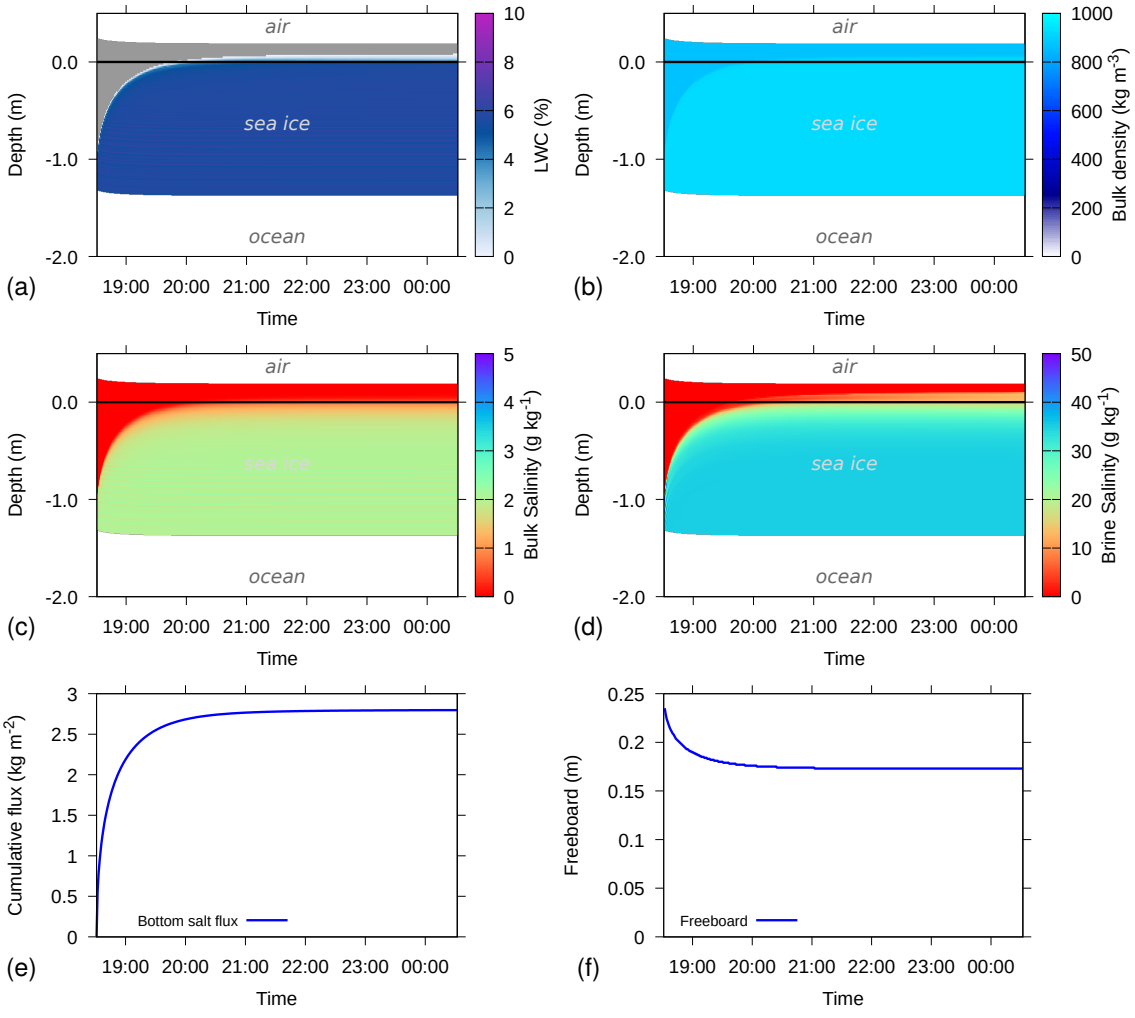

Figure 2. Example simulation where initially dry sea ice with 94% volumetric ice content is placed into ocean water with a salinity of 35 g kg^{-1}. Shown are (a) liquid water content (LWC), (b) bulk density, (c) bulk salinity, (d) brine salinity, (e) cumulative salt flux at the bottom of the sea ice and (f) freeboard. In (a), dry snow is colored grey. In (a), (b), (c), and (d), the depth on the y-axis is relative to sea level, i.e., sea level is 0 and indicated by the solid black line.

4.2 Temperature validation

Fig. 3a and 3b show the simulated temperature of the snow–sea ice system for simulations driven by in-situ measured snow depth and ERA5 precipitation, respectively. Dashed lines denote the reference level, i.e., the snow–sea ice interface as determined upon installation of the Snow Buoy. The sea level as calculated from hydrostatic balance is indicated by the solid line. The sea level stays below the snow–sea ice interface, i.e., freeboard is positive in the simulations during the whole simulation period.

Geosci. Model Dev. Discuss., https://doi.org/10.5194/gmd-2019-97
Manuscript under review for journal Geosci. Model Dev.
Discussion started: 14 May 2019

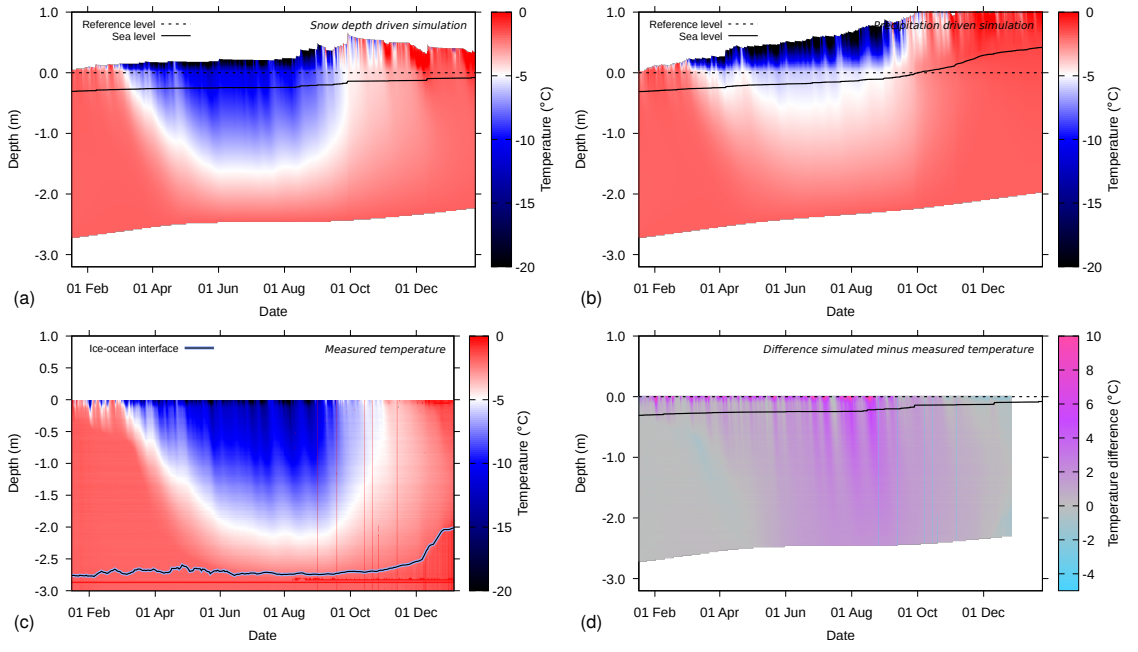

Figure 3. Snow and ice temperatures for Snow Buoy 2016S31 / IMB 2016T41, in (a) simulations driven by in-situ measured snow depth, (b) simulations driven by ERA5 precipitation, (c) measured temperatures by the IMB and (d) the difference between simulated (driven by snow depth) and measured temperatures. The depth on the y-axis is defined relative to the sea ice-snow interface, as determined upon installation (dashed line). The solid line denotes the simulated sea level.

Fig. 3c shows the measured sea ice temperatures from the corresponding IMB. Note that for this IMB, the thermistor string does not extend above the initial 2 cm snow layer on top of the sea ice, such that the time evolution of the snow cover is not recorded by the IMB. We find that the IMB confirms the strong cooling of the sea ice during the austral winter months, as found in the simulations, as well as the near-surface warming to the melting point of fresh water shortly before the last transmission by the buoy.

Fig 3d shows the difference between measured temperatures and the simulated temperatures in the ice by the snow depth driven simulations (i.e., Fig 3c minus Fig. 3a), with positive values denoting an overestimated temperature by the model and vice versa. The comparison shows that in spring, the simulation slightly underestimates the sea ice temperatures, which suggests an overestimation of the initial cooling of the sea ice during the austral winter months. The model underestimates the lowest temperatures reached in winter by up to 6-10°C near the snow–sea ice interface, which is located at the top of the thermistor string. Similarly, incidental cooling in near surface sea ice layers in February and March are also underestimated. This could indicate an overestimation of the surface energy balance by the model, but also by an underestimated new snow density, and thus underestimated thermal conductivity, by the model.

The thermistor string is also used to determine the heat capacity by heating the string for 1 or 2 minutes and looking at the temperature response. By combining the absolute temperatures and the heating rates, the ice–ocean interface has been

determined as shown in Fig. 3c. The IMB data confirm the modelling result that the strong negative energy balance at the top of the snow–sea ice system during austral winter has not resulted in an ice thickness increase. The decrease in ice thickness in December 2016 is not reproduced by the model. The trajectory of the buoy shows a marked change in drift direction (Fig. 1), changing from a northward to a southward drifting during this period. This change of direction may have been accompanied by an intrusion of warm ocean water below the sea ice and an increased ocean heat flux.

Fig. 3a and 3b show the simulation driven by in-situ snow depth measurements, and by precipitation time series from ERA5, respectively. The in-situ measured snow depth on the Snow Buoys qualitatively shows a good agreement in terms of timing of precipitation events and the general evolution of the snow cover on the sea ice. However, the ERA5 precipitation leads to accumulations in the austral winter time, that are not present in the snow depth time series. This is not necessary a bias in ERA5, because snow erosion by wind can keep the snow depth constant over extended periods of time. Due to this discrepancy, the total snow depth is slightly overestimated by the ERA5 input at the end of the simulation.

LWC, bulk and brine salinity, as well as the bottom salt flux for the simulations driven by measured snow depth are shown in Fig. 4. LWC (Fig. 4a) shows a strong reduction in austral winter due to the freezing brine. In December, occasional surface meltwater from the snow percolates down in the sea ice. Combined with rising temperatures, a high LWC layer forms around and just below sea level. Fig. 4b shows that the bulk salinity of the sea ice hardly changes over the course of the simulation, whereas the brine salinity (Fig. 4c) clearly shows a relationship with the temperature. This reflects the prescribed thermal equilibrium between brine and the ice, assuming that the brine is at melting temperature. Fig. 4d shows that the added weight of snow accumulation pushes the sea ice deeper into the ocean, increasing the pressure head at the bottom of the sea ice. This leads to an influx of saline water.

4.3 Fixed Salinity Profiles

In Fig. 5, we show an example of a simulation with a prescribed, time-invariant salinity profile. The bulk salinity profile is fixed between the bottom and top of the sea ice, with a value of 12 g kg^{-1}. The vertical distribution of bulk salinity is then prescribed by a sine function with an amplitude of 8 g kg^{-1}. The snow is assigned a constant salinity of 1 g kg^{-1}. The water transport is described by the bucket scheme, which is the only scheme that works with prescribed salinity profiles.

The salinity in snow causes the presence of some amount of liquid water in the snowpack, such that the brine salinity satisfies the melting point temperature. We also find that the high bulk salinity prescribed near the snow – ice interface requires high values of LWC to arrive at the brine salinity that would correspond to the ice temperatures. The latent heat required for melting of ice to achieve this, results in lower temperatures of the sea ice. Overall, the simulations compare well to simulations with explicit salinity transport, in terms of ice thickness and temperature distributions.

4.4 Flooding and Superimposed Ice Formation

Figs. 6 and 7 show an example simulation for Snow Buoy 2014S12. The simulations were driven by the snow depth measurements from the buoy. Upon installation of the buoy, the snow depth was referenced to the sea ice surface. This reference level is shown by the dashed line. Due to basal ice melt and growth, as well as additional snowfall, the simulated sea level became

Geosci. Model Dev. Discuss., https://doi.org/10.5194/gmd-2019-97
Manuscript under review for journal Geosci. Model Dev.
Discussion started: 14 May 2019

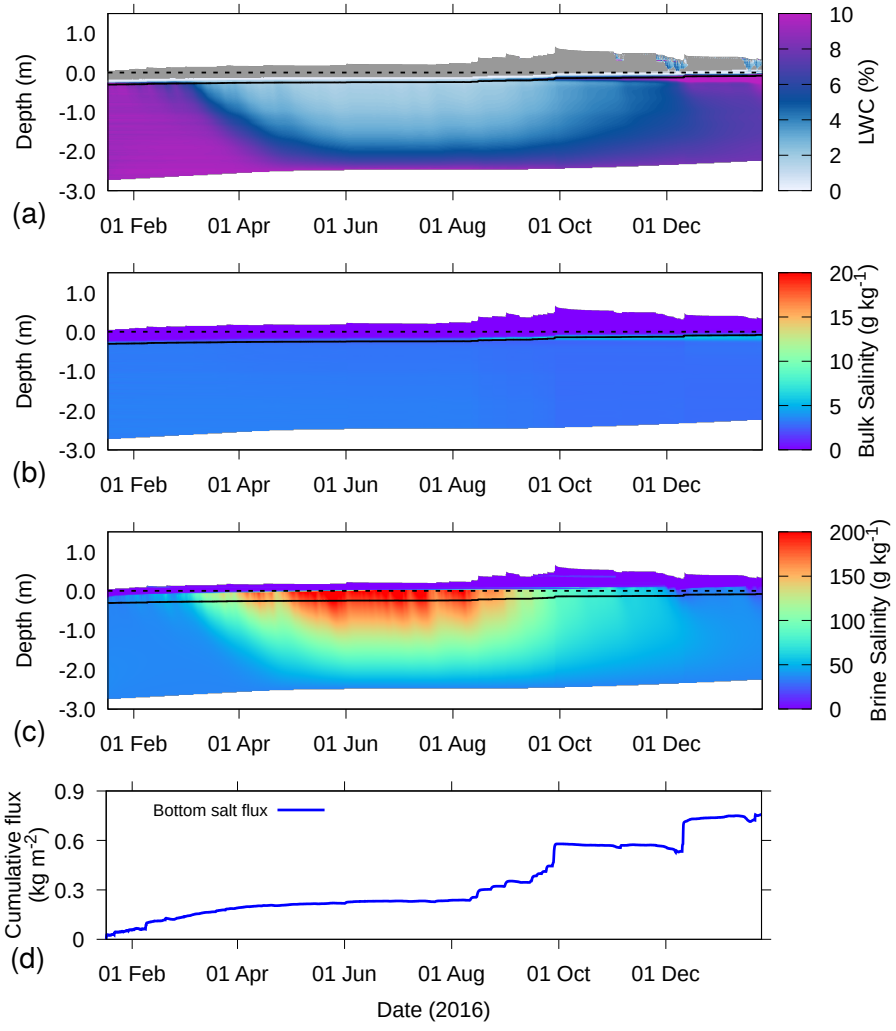

Figure 4. Example simulation for Snow Buoy 2016S31, where measured snow depth was used to derive the precipitation events, for temperature (a), LWC (b), bulk salinity (c), brine salinity (d) and cumulative salt flux at the bottom of the sea ice (e). In (b), dry snow is colored grey. In (a), (b), and (c), the depth is defined relative to the sea ice-snow interface, as determined upon installation (dashed line). The solid line denotes the sea level as determined by the simulations. An increasing cumulative flux denotes inflow and vice versa.

higher w.r.t. to the snow depth sensor, as indicated by the solid line. This is congruent with a negative freeboard. It indicates that significant flooding occurred, as also evidenced by the LWC in Fig. 6b and associated high bulk salinity (Fig. 6c). Fig. 7b shows that much of the sea water that flooded the snow refroze, adding substantial ice mass.

Fig. 6e shows that flooding also leads to a strong influx of salt to the snow-sea ice system. The flooding saturates the snow, which has significant pore space compared to the sea ice. Therefore, snowfall events of similar magnitude have different effects on the salt influx, depending whether or not flooding occurs at the time.

Geosci. Model Dev. Discuss., https://doi.org/10.5194/gmd-2019-97
Manuscript under review for journal Geosci. Model Dev.
Discussion started: 14 May 2019

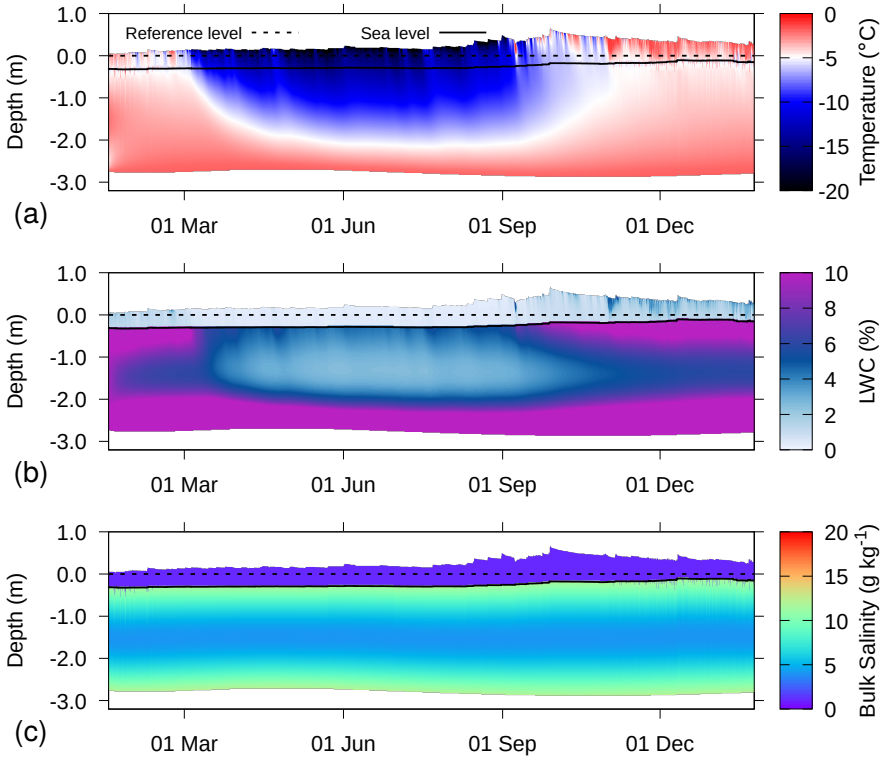

Figure 5. Example simulation for buoy 2016S31, where measured snow depth was used to derive the precipitation events, and the bulk salinity profile was prescribed, for temperature (a), LWC (b) and bulk salinity (c). In (b), dry snow is colored grey. The depth on the y-axis is defined relative to the sea ice-snow interface, as determined upon installation (dashed line). The solid line denotes the sea level as determined by the simulations.

Note that the flooding, as depicted in simulations with the Richards equation coupled to the transport equation, is governed by the hydraulic conductivity of ice. In cold ice, hydraulic conductivity can be so low that negative freeboard remains for extended period of times, even without flooding. On the other hand, flooding may also be triggered by deformation and cracking of the sea ice, combined with lateral flow effects. However, Maksym and Jeffries (2000) have shown that the simpler assumption (i.e., negative freeboard will trigger flooding) can already yield satisfying results. In the model, the maximum ice contents is fixed to 0.99 m^3 m^{-3}, such that hydraulic conductivity is typically large enough for instantaneous flooding.

4.5 Forced Warming and Cooling

We used Snow Buoy 2016S31 for two experiments where we forced constant warming and constant cooling conditions by modifying the meteorological driving data starting April 1, 2016. For warming, we prescribed a constant air temperature of +5 °C, a wind speed of 3 m s^{-1} and an incoming shortwave radiation of 300 W m^{-2}.

Geosci. Model Dev. Discuss., https://doi.org/10.5194/gmd-2019-97
Manuscript under review for journal Geosci. Model Dev.
Discussion started: 14 May 2019

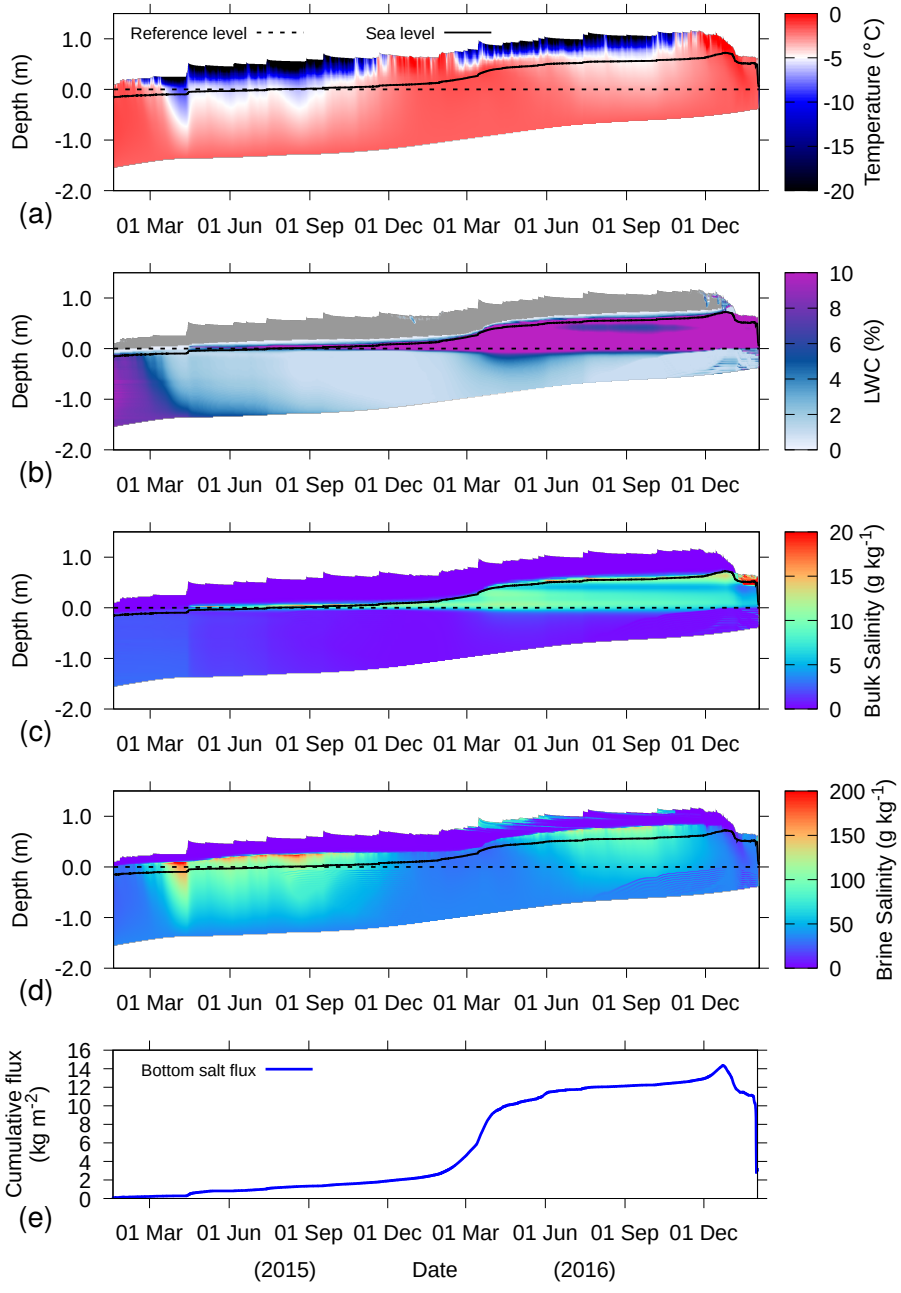

Figure 6. Example simulation for buoy 2014S12, where measured snow depth was used to derive the precipitation events, for temperature (a), LWC (b), bulk salinity (c), brine salinity (d) and cumulative salt flux at the bottom of the sea ice (e). In (b), dry snow is colored grey. In (a), (b), (c), and (d), the depth is defined relative to the sea ice-snow interface, as determined upon installation (dashed line). The solid line denotes the sea level as determined by the simulations. An increasing cumulative flux denotes inflow and vice versa.

Geosci. Model Dev. Discuss., https://doi.org/10.5194/gmd-2019-97
Manuscript under review for journal Geosci. Model Dev.
Discussion started: 14 May 2019

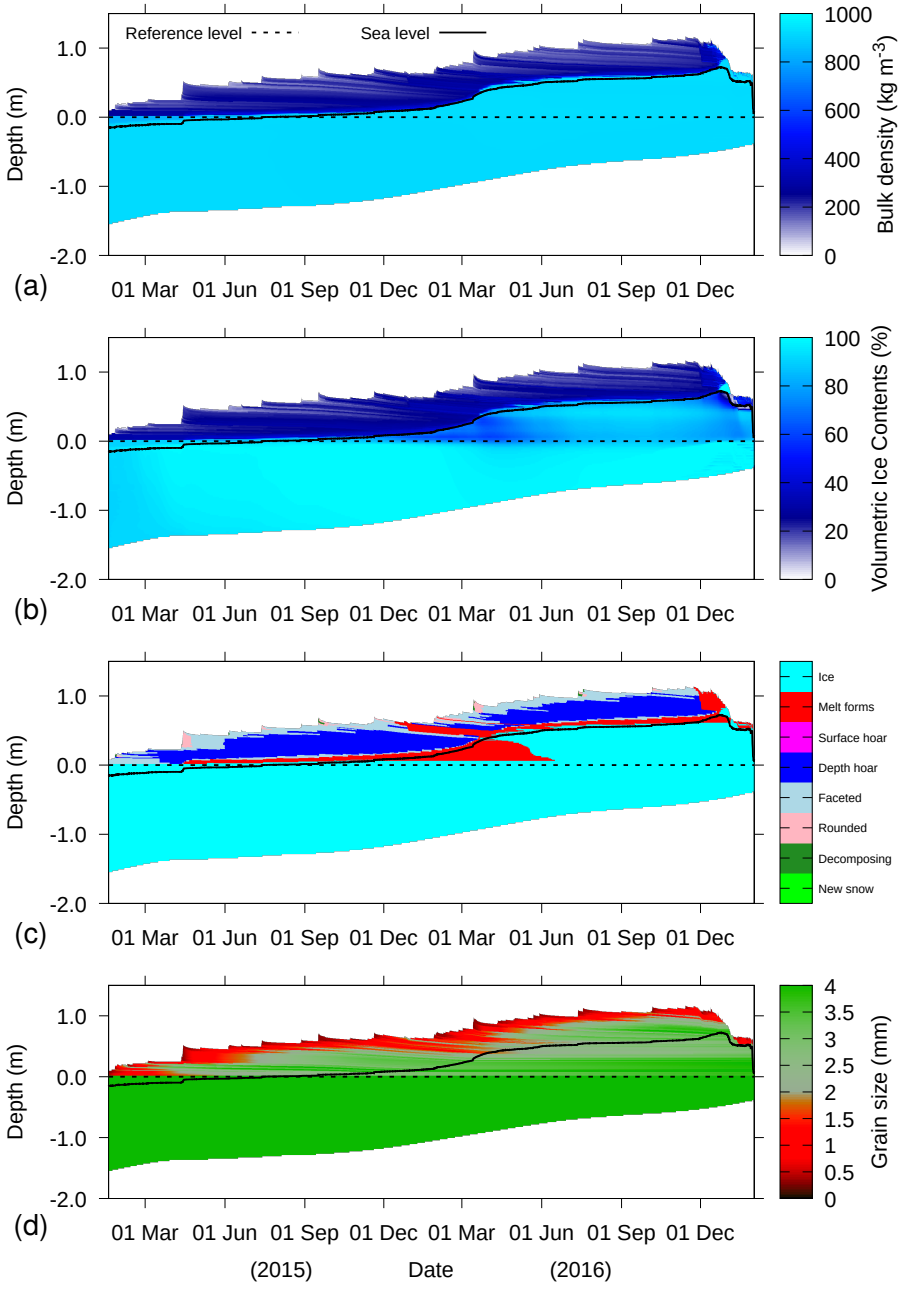

Figure 7. Example simulation for buoy 2014S12, where measured snow depth was used to derive the precipitation events, for total bulk density (a), volumetric ice content (b), grain type (c) and grain size (d). The depth on the y-axis is defined relative to the sea ice-snow interface, as determined upon installation (dashed line). The solid line denotes the sea level as determined by the simulations.

Geosci. Model Dev. Discuss., https://doi.org/10.5194/gmd-2019-97
Manuscript under review for journal Geosci. Model Dev.
Discussion started: 14 May 2019

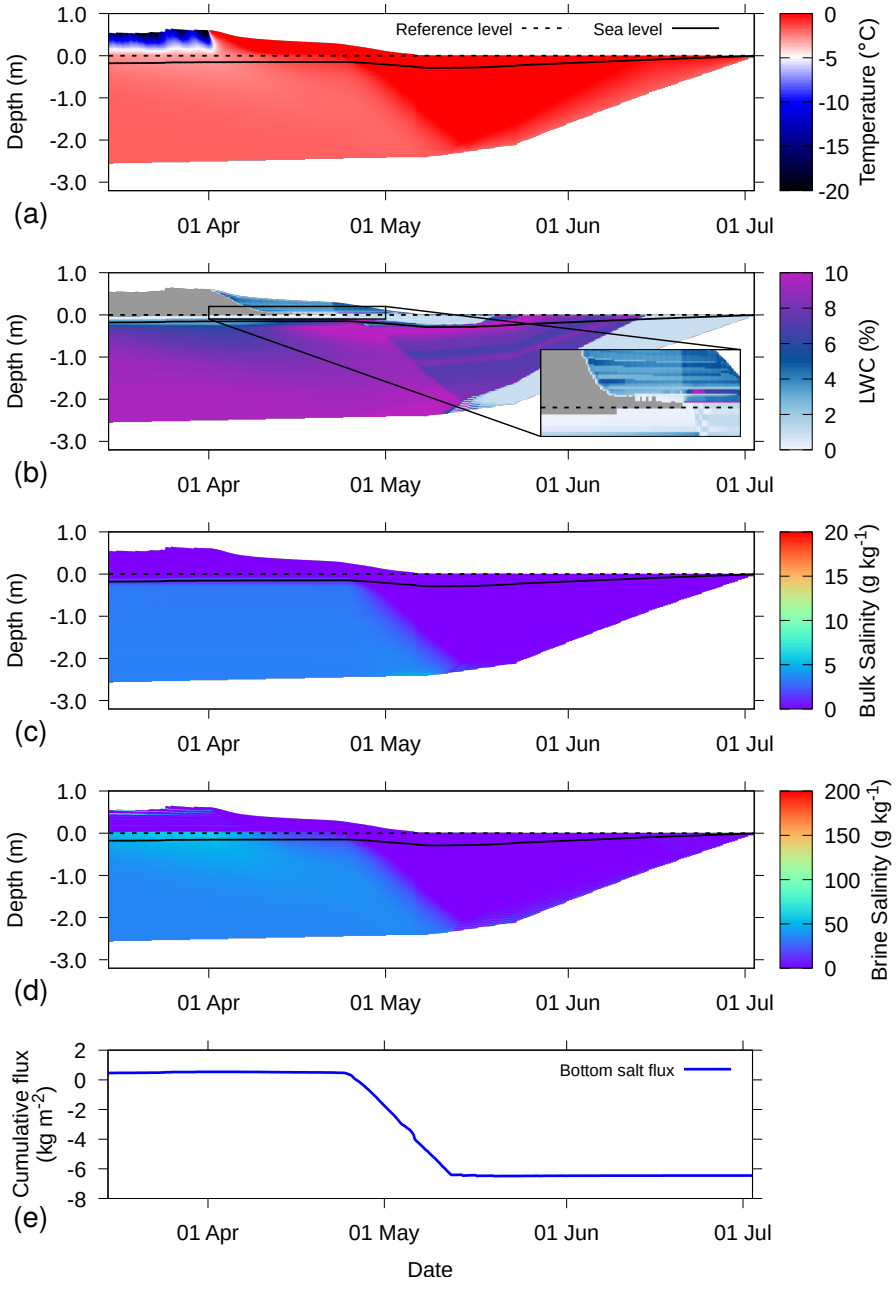

Figure 8. Simulation for 2016S31, where from April 1 onward, melting conditions are enforced, for temperature (a), LWC (b), bulk salinity (c), brine salinity (d) and cumulative salt flux at the bottom of the sea ice (e). In (b), dry snow is colored grey. In (a), (b), (c), and (d), the depth on the y-axis is defined relative to the sea ice-snow interface, as determined upon installation (dashed line). The solid line denotes the sea level as determined by the simulations. An increasing cumulative flux denotes inflow and vice versa.

Geosci. Model Dev. Discuss., https://doi.org/10.5194/gmd-2019-97
Manuscript under review for journal Geosci. Model Dev.
Discussion started: 14 May 2019

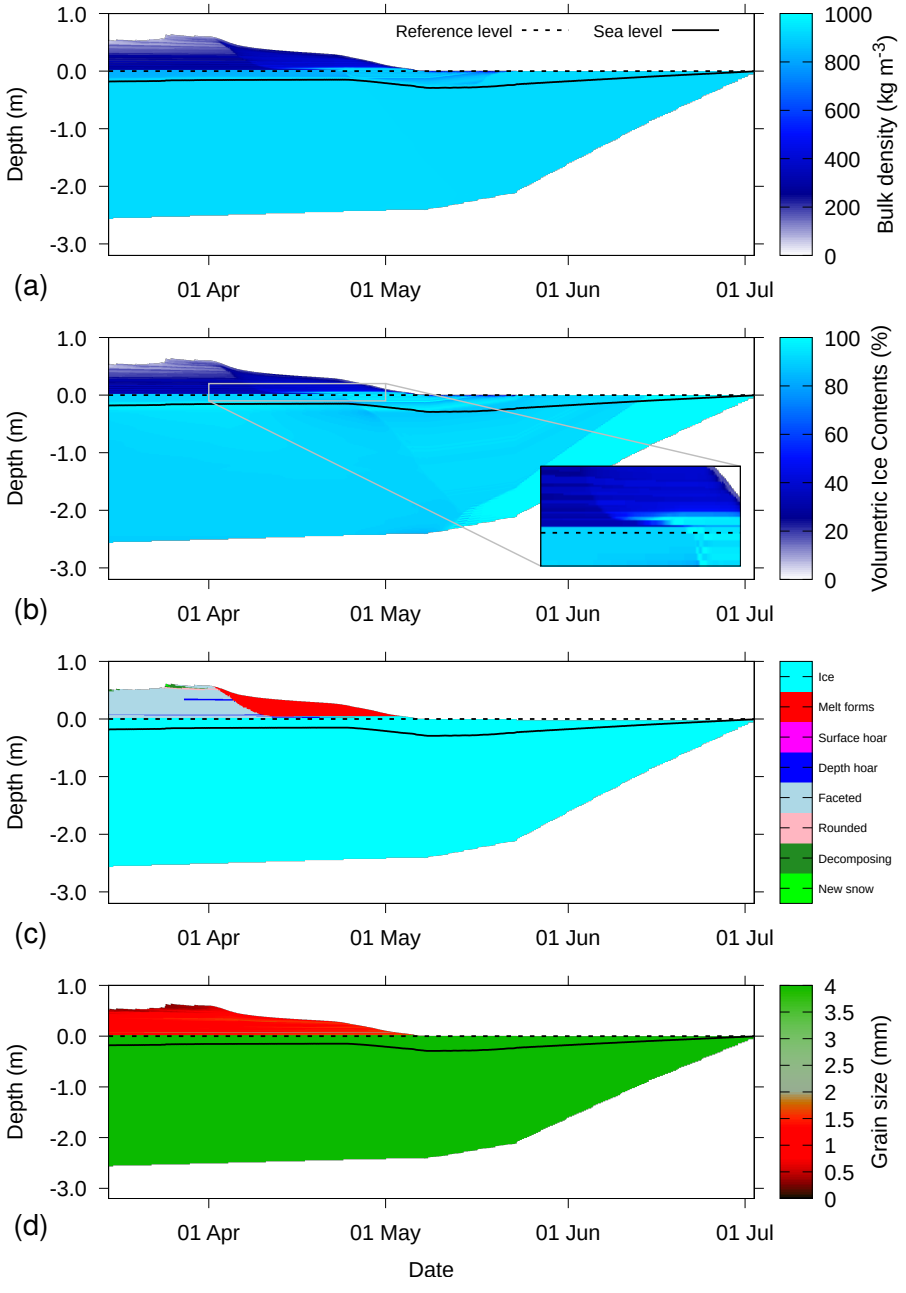

Figure 9. Simulation for 2016S31, where from April 1 onward, melting conditions are enforced, for total bulk density (a), volumetric ice content (b), grain type (c) and grain size (d). The depth on the y-axis is defined relative to the sea ice-snow interface, as determined upon installation (dashed line). The solid line denotes the sea level as determined by the simulations.

Geosci. Model Dev. Discuss., https://doi.org/10.5194/gmd-2019-97
Manuscript under review for journal Geosci. Model Dev.
Discussion started: 14 May 2019

Fig. 8 and 9 show the warming example of buoy 2016S31. The fresh water percolating as a result from snow melt first starts accumulating on below-freezing sea ice with low porosity (see Fig. 8b). This process is visible between April 14 and April 27 and leads to superimposed ice formation (Fig. 9b and 9c). Upon continued warming, fresh water starts flushing the ice, leading to a rapid reduction of bulk and brine salinity (Fig. 8c,d).

Fig. 10 shows an example where cooling conditions were enforced. Similar to the warming example, the meteorological forcing conditions were replaced from April 1 onward by setting a constant air temperature of -30 °C, a wind speed of 1 m s^{-1} and no incoming shortwave radiation. The ocean heat flux was set at 8 W m^{-2}. We find a consistent cooling and increase in brine salinity (Fig. 10d). This is achieved by freezing the liquid water, as shown by the decrease in LWC (Fig. 10b). The bulk salinity remains approximately constant (Fig. 10c).

An increase in brine salinity also increases the density of the brine. This may lead to flushing of the sea ice, when the heavy brine moves downward and is replaced by lighter ocean water. However, in our simulations, there is only a very small outflow of salinity at the bottom ((Fig. 10e). This result shows that without a description of the convective processes in sea ice resulting from cooling (Griewank and Notz, 2013), the salinity depletion found due to cooling is strongly underestimated by this model approach.

4.6 Thin Ice

A final test is run by starting with only 2 cm of ice, with constant atmospheric conditions to simulate thin ice evolution. The atmospheric conditions were set as -10 °C air temperature, 100% relative humidity, no wind speed, no incoming solar radiation and a constant incoming longwave radiation of 230 W m^{-2}. The ocean heat flux was set to 0 W m^{-2}.

The simulations were run for 1 month, which resulted in approximately 50 cm ice growth (Fig. 11). The relatively warm sea ice compared to the air temperature results in a latent heat flux directed to the atmosphere, even though relative humidity is 100%. The evaporation at the top of the sea ice leads to an outflow of fresh water at the top of the snowpack, resulting in an accumulation of salt near the surface (Kaleschke et al., 2004; Domine et al., 2005, e.g.). The transport of salt from below decreases with increasing ice thickness, as capillary forces are not strong enough anymore to bridge the freeboard.

5 Conclusions

We introduced a series of modifications to the physics-based, multi-layer SNOWPACK model to allow it to simulate sea ice. This involved modifying the model thermodynamics to account for the varying melting point of ice based on salinity and adding domain restructuring to allow basal ice growth. Water transport through the snow – sea ice system can optionally be described by the Richards equation, which describes water flow in porous media for the full range from saturated conditions (Darcy law) to unsaturated conditions. This equation is coupled to a concentration equation for salinity. With the adapted model, we explicitly describe several aspects of brine dynamics, such as flooding, superimposed ice formation and the percolation of fresh water from snow melt, flushing the sea ice. The model formulations allow for a certain amount of drainage of dense brine, but

Geosci. Model Dev. Discuss., https://doi.org/10.5194/gmd-2019-97
Manuscript under review for journal Geosci. Model Dev.
Discussion started: 14 May 2019

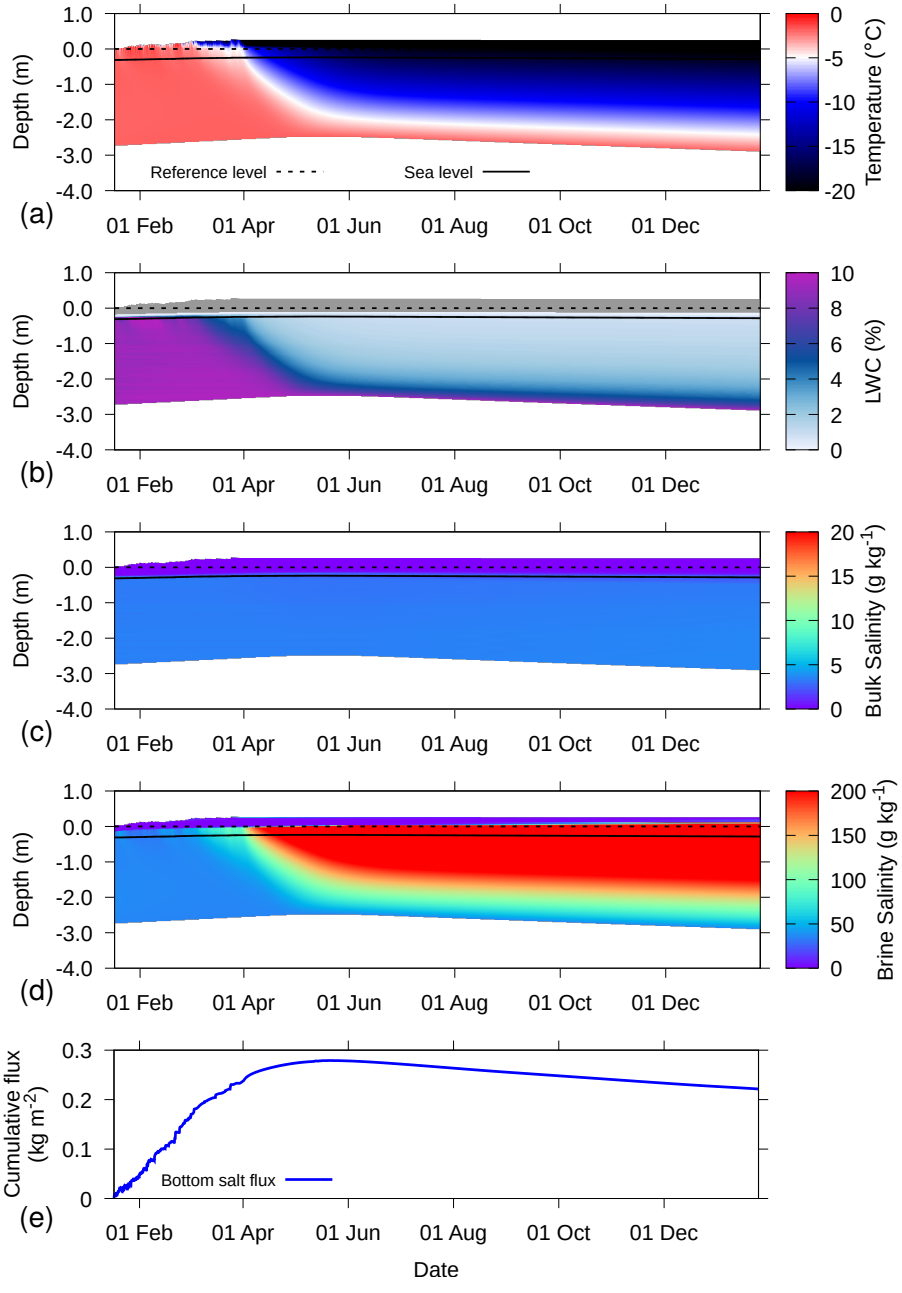

Figure 10. Simulation for 2016S31, where from April 1 onward, cooling conditions are enforced, for temperature (a), LWC (b), bulk salinity (c), brine salinity (d) and cumulative salt flux at the bottom of the sea ice (e). In (b), dry snow is colored grey. In (a), (b), (c), and (d), the depth on the y-axis is defined relative to the sea ice-snow interface, as determined upon installation (dashed line). The solid line denotes the sea level as determined by the simulations. An increasing cumulative flux denotes inflow and vice versa.

Geosci. Model Dev. Discuss., https://doi.org/10.5194/gmd-2019-97
Manuscript under review for journal Geosci. Model Dev.
Discussion started: 14 May 2019

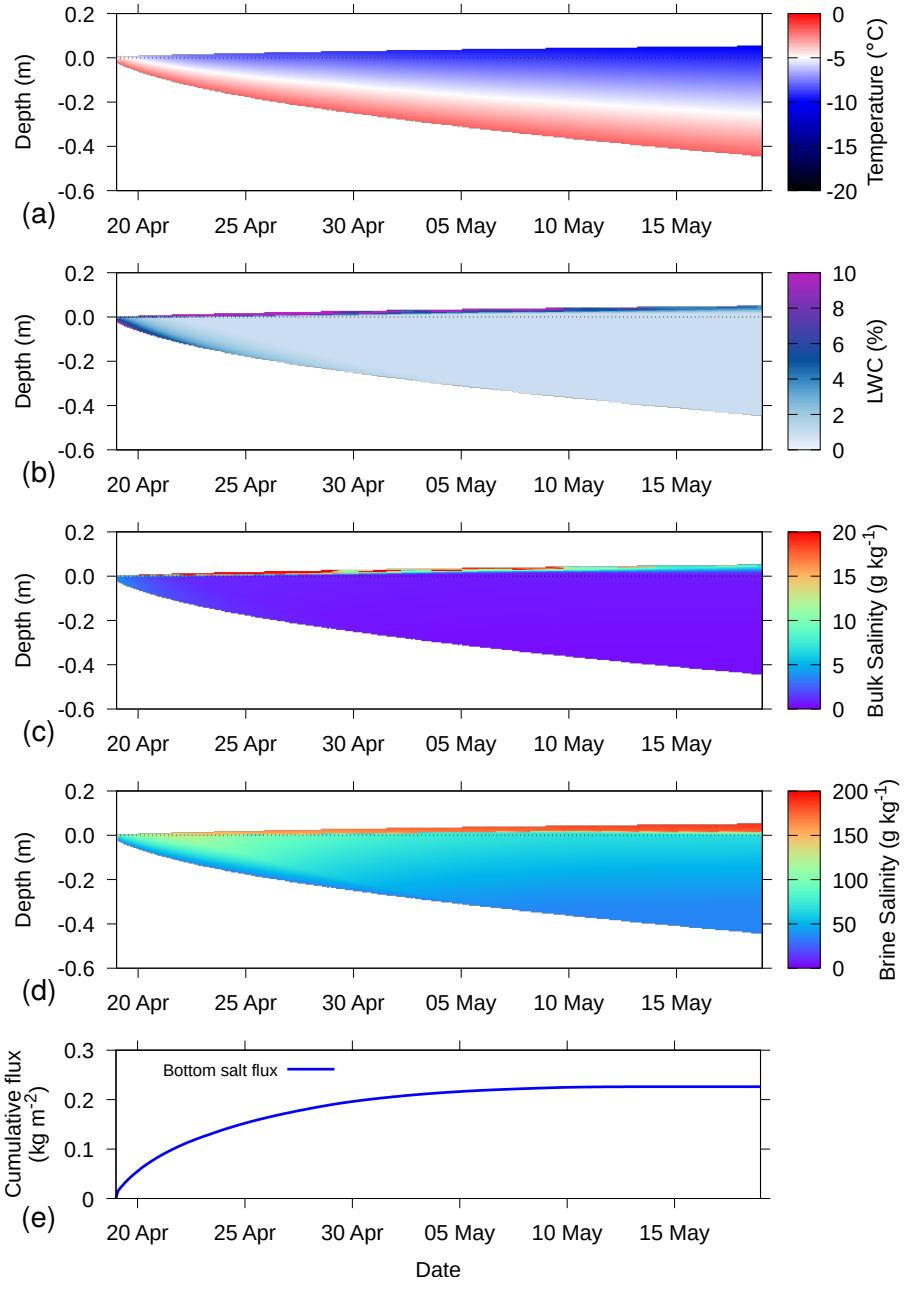

Figure 11. Simulation for 2016S31, where from April 1 onward, melting conditions is enforced, for temperature (a), LWC (b), bulk salinity (c), brine salinity (d) and cumulative salt flux at the top and bottom of the sea ice (e). In (b), dry snow is colored grey. In (a), (b), (c), and (d), the depth on the y-axis is defined relative to sea level. An increasing cumulative flux denotes inflow and vice versa.

the process is largely underestimated compared to what is known from literature, as convective brine transport is, thus far, not described by the model.

The modifications allow the snow microstructure descriptions developed in the SNOWPACK model to be applied for sea ice conditions as well. The model is able to simulate the temporal evolution of snow density, grain size and shape and snow wetness over the life span of an ice floe. We find abundant depth hoar layers and melt layers, as well as superimposed ice formation due to flooding and percolation.

Driving the simulations, particularly estimating the ocean heat flux from below, is difficult due to limited forcing data from polar regions. Simulations based on Snow and IMB Buoy data demonstrate the importance of such remote data collection systems for modelling. The detailed snow microstructure evolution can be used for remote sensing retrieval algorithms to assess snow depth and ice thickness from space. For this, a coupling to the Snow Microwave Radiative Transfer model SMRT (Picard et al., 2018) is foreseen.

Code and data availability. The SNOWPACK model and the MeteoIO meteorological preprocessing library (Bavay and Egger, 2014) needed to run SNOWPACK are available under a LGPLv3 license under https://models.slf.ch. The source code of the version used for the simulations presented in this study corresponds to revision 2380 of MeteoIO (https://models.slf.ch/svn/meteoio/trunk) and revision 1751 of SNOWPACK (https://models.slf.ch/svn/snowpack/branches/dev). The input and configuration files for the example simulations in this study are available as an Online Supplement. The website https://niviz.org/ can be used to visualize the SNOWPACK output files.
The Snow Buoy and IMB data are available at http://www.meereisportal.de (direct link to data archive: http://data.meereisportal.de/gallery/index_new.php?lang=en_US&active-tab1=method&active-tab2=buoy).

Author contributions. NW developed the model code and performed the simulations, LR performed code testing, LR, NM, KL, LK, MN and ML contributed to model conceptualization and design. NW prepared the manuscript with contributions from all co-authors.

Acknowledgements

We thank the captain, officers and crew of R/V Polarstern for their support during the campaigns to deploy the Snow Bouys and IMBs. Louisa von Hülsen from the Alfred Wegener Institute is acknowledged for providing preliminary IMB analysis data. N.W. was supported by the Swiss National Science Foundation (SNSF), grant no. P2ELP2_172299. This work was additionally supported by the US National Science Foundation (NSF) grant no. OPP-1142075 and Swiss National Science Foundation grant no. PZ00P2_142684. We also thank the German Research Council (DFG) for funding the Snow cover impacts on Antarctic Sea Ice (SCASI) project within the framework of the priority program "Antarctic Research with comparative investigations in Arctic ice areas" (grant no: NI 1096/5-1 and KA 2694/7-1). The Helmholtz infrastructure programs FRAM and ACROSS is acknowledged for funding the Snow and Ice Mass-balance Buoys. ERA5 data constitute modified Copernicus Climate Change Service Information [2018].

References

Ackley, S. F., Xie, H., and Tichenor, E. A.: Ocean heat flux under Antarctic sea ice in the Bellingshausen and Amundsen Seas: two case studies, Ann. Glaciol., 56, 200–210, https://doi.org/10.3189/2015AoG69A890, 2015.

Allison, I., Brandt, R. E., and Warren, S. G.: East Antarctic sea ice: Albedo, thickness distribution, and snow cover, J. Geophys. Res., 98, 12 417–12 429, https://doi.org/10.1029/93JC00648, http://dx.doi.org/10.1029/93JC00648, 1993.

Anderson, E., Bai, Z., Bischof, C., Blackford, S., Demmel, J., Dongarra, J., Du Croz, J., Greenbaum, A., Hammarling, S., McKenney, A., and Sorensen, D.: LAPACK Users' Guide, Society for Industrial and Applied Mathematics, Philadelphia, PA, third edn., 1999.

Andreas, E. L.: Parameterizing Scalar Transfer over Snow and Ice: A Review, J. Hydrometeor., 3, 417–432, https://doi.org/10.1175/1525-7541(2002)003<0417:PSTOSA>2.0.CO;2, 2002.

Assur, A.: Composition of sea ice and its tensile strength, Research report 44, U.S. Army Snow, Ice and Permafrost Research Establishment, Corps of Engineers, Wilmette, Ill., 1960.

Bartelt, P. and Lehning, M.: A physical SNOWPACK model for the Swiss avalanche warning Part I: Numerical model, Cold Reg. Sci. Technol., 35, 123–145, https://doi.org/10.1016/S0165-232X(02)00074-5, 2002.

Bavay, M. and Egger, T.: MeteoIO 2.4.2: a preprocessing library for meteorological data, Geosci. Model Dev., 7, 3135–3151, https://doi.org/10.5194/gmd-7-3135-2014, http://www.geosci-model-dev.net/7/3135/2014/, 2014.

Bitz, C. M. and Lipscomb, W. H.: An energy-conserving thermodynamic model of sea ice, J. Geophys. Res., 104, 15 669–15 677, https://doi.org/10.1029/1999JC900100, http://dx.doi.org/10.1029/1999JC900100, 1999.

Brandt, R. E., Warren, S. G., Worby, A. P., and Grenfell, T. C.: Surface Albedo of the Antarctic Sea Ice Zone, J. Climate, 18, 3606–3622, https://doi.org/10.1175/JCLI3489.1, https://doi.org/10.1175/JCLI3489.1, 2005.

Calonne, N., Flin, F., Morin, S., Lesaffre, B., du Roscoat, S. R., and Geindreau, C.: Numerical and experimental investigations of the effective thermal conductivity of snow, Geophys. Res. Lett., 38, L23 501, https://doi.org/10.1029/2011GL049234, 2011.

Calonne, N., Geindreau, C., Flin, F., Morin, S., Lesaffre, B., Rolland du Roscoat, S., and Charrier, P.: 3-D image-based numerical computations of snow permeability: links to specific surface area, density, and microstructural anisotropy, Cryosphere, 6, 939–951, https://doi.org/10.5194/tc-6-939-2012, 2012.

Celia, M. A., Bouloutas, E. T., and Zarba, R. L.: A general mass-conservative numerical solution for the unsaturated flow equation, Water Resour. Res., 26, 1483–1496, https://doi.org/10.1029/WR026i007p01483, 1990.

Chung, Y.-C., Bélair, S., and Mailhot, J.: Simulation of Snow on Arctic Sea Ice Using a Coupled Snow–Ice Model, J. Hydrometeor., 11, 199–210, https://doi.org/10.1175/2009JHM1112.1, https://doi.org/10.1175/2009JHM1112.1, 2010.

Crank, J. and Nicolson, P.: A practical method for numerical evaluation of solutions of partial differential equations of the heat-conduction type, Advances in Computational Mathematics, 6, 207–226, https://doi.org/10.1007/BF02127704, https://doi.org/10.1007/BF02127704, 1996.

Déry, S. J. and Tremblay, L.-B.: Modeling the Effects of Wind Redistribution on the Snow Mass Budget of Polar Sea Ice, J. Phys. Oceanogr., 34, 258–271, https://doi.org/10.1175/1520-0485(2004)034<0258:MTEOWR>2.0.CO;2, 2004.

Domine, F., Sparapani, R., Ianniello, A., and Beine, H. J.: The origin of sea salt in snow on Arctic sea ice and in coastal regions, Atmos. Chem. Phys., 4, 2259–2271, https://doi.org/10.5194/acp-4-2259-2004, 2004.

Domine, F., Taillandier, A. S., Simpson, W. R., and Severin, K.: Specific surface area, density and microstructure of frost flowers, Geophys. Rese. Lett., 32, L13 502, https://doi.org/10.1029/2005GL023245, https://agupubs.onlinelibrary.wiley.com/doi/abs/10.1029/2005GL023245, 2005.

Eicken, H., Lange, M. A., and Wadhams, P.: Characteristics and distribution patterns of snow and meteoric ice in the Weddell Sea and their contribution to the mass balance of sea ice, Ann. Geophys., 12, 80–93, https://doi.org/10.1007/s00585-994-0080-x, http://dx.doi.org/10.1007/s00585-994-0080-x, 1994.

Eicken, H., Fischer, H., and Lemke, P.: Effects of the snow cover on Antarctic sea ice and potential modulation of its response to climate change, Ann. Glaciol., 21, 369–376, https://doi.org/10.3189/S0260305500016086, 1995.

Ferrari, R., Jansen, M. F., Adkins, J. F., Burke, A., Stewart, A. L., and Thompson, A. F.: Antarctic sea ice control on ocean circulation in present and glacial climates, PNAS, https://doi.org/10.1073/pnas.1323922111, http://www.pnas.org/content/early/2014/05/29/1323922111, 2014.

Fuller, M. C., Geldsetzer, T., Yackel, J., and Gill, J. P. S.: Comparison of a coupled snow thermodynamic and radiative transfer model with in situ active microwave signatures of snow-covered smooth first-year sea ice, Cryosphere, 9, 2149–2161, https://doi.org/10.5194/tc-9-2149-2015, https://www.the-cryosphere.net/9/2149/2015/, 2015.

Golden, K. M., Eicken, H., Heaton, A. L., Miner, J., Pringle, D. J., and Zhu, J.: Thermal evolution of permeability and microstructure in sea ice, Geophys. Res. Lett., 34, https://doi.org/10.1029/2007GL030447, https://agupubs.onlinelibrary.wiley.com/doi/abs/10.1029/2007GL030447, 2007.

Goosse, H. and Fichefet, T.: Importance of ice-ocean interactions for the global ocean circulation: A model study, J. Geophys. Res., 104, 23 337–23 355, https://doi.org/10.1029/1999JC900215, https://agupubs.onlinelibrary.wiley.com/doi/abs/10.1029/1999JC900215, 1999.

Gordon, A. L.: The Southern-Ocean and Global Climate, Oceanus, 31, 39–46, 1988.

Grenfell, T. C. and Perovich, D. K.: Spectral albedos of sea ice and incident solar irradiance in the southern Beaufort Sea, J. Geophys. Res., 89, 3573–3580, https://doi.org/10.1029/JC089iC03p03573, https://agupubs.onlinelibrary.wiley.com/doi/abs/10.1029/JC089iC03p03573, 1984.

Griewank, P. J. and Notz, D.: Insights into brine dynamics and sea ice desalination from a 1-D model study of gravity drainage, J. Geophys. Res., 118, 3370–3386, https://doi.org/10.1002/jgrc.20247, 2013.

Groot Zwaaftink, C. D., Cagnati, A., Crepaz, A., Fierz, C., Macelloni, G., Valt, M., and Lehning, M.: Event-driven deposition of snow on the Antarctic Plateau: analyzing field measurements with SNOWPACK, Cryosphere, 7, 333–347, https://doi.org/10.5194/tc-7-333-2013, 2013.

Grosfeld, K., Treffeisen, R., Asseng, J., Bartsch, A., Bräuer, B., Fritzsch, B., Gerdes, R., Hendricks, S., Hiller, W., Heygster, G., Krumpen, T., Lemke, P., Melsheimer, C., Nicolaus, M., Ricker, R., and Weigelt, M.: Online sea-ice knowledge and data platform <www.meereisportal.de>, Polarforschung, 85, 143–155, https://doi.org/10.2312/polfor.2016.011, 2015.

Haas, C., Thomas, D. N., and Bareiss, J.: Surface properties and processes of perennial Antarctic sea ice in summer, J. Glaciol, 47, 613–625, https://doi.org/10.3189/172756501781831864, 2001.

Haas, C., Beckers, J., King, J., Silis, A., Stroeve, J., Wilkinson, J., Notenboom, B., Schweiger, A., and Hendricks, S.: Ice and Snow Thickness Variability and Change in the High Arctic Ocean Observed by In Situ Measurements, Geophys. Res. Lett., 44, 10,462–10,469, https://doi.org/10.1002/2017GL075434, https://agupubs.onlinelibrary.wiley.com/doi/abs/10.1002/2017GL075434, 2017.

Hunke, E. C., Notz, D., Turner, A. K., and Vancoppenolle, M.: The multiphase physics of sea ice: a review for model developers, Cryosphere, 5, 989–1009, https://doi.org/10.5194/tc-5-989-2011, https://www.the-cryosphere.net/5/989/2011/, 2011.

Huwald, H., Tremblay, L.-B., and Blatter, H.: A multilayer sigma-coordinate thermodynamic sea ice model: Validation against Surface Heat Budget of the Arctic Ocean (SHEBA)/Sea Ice Model Intercomparison Project Part 2 (SIMIP2) data, J. Geophys. Res., 110, C05 010, https://doi.org/10.1029/2004JC002328, https://agupubs.onlinelibrary.wiley.com/doi/abs/10.1029/2004JC002328, 2005.

Jackson, K., Wilkinson, J., Maksym, T., Meldrum, D., Beckers, J., Haas, C., and Mackenzie, D.: A Novel and Low-Cost Sea Ice Mass Balance Buoy, J. Atmos. Ocean Technol., 30, 2676–2688, https://doi.org/10.1175/JTECH-D-13-00058.1, https://doi.org/10.1175/JTECH-D-13-00058.1, 2013.

Jeffries, M. O., Morris, K., Weeks, W., and Worby, A. P.: Seasonal variations in the properties and structural composition of sea ice and snow cover in the Bellingshausen and Amundsen Seas, Antarctica, J. Glaciol., 43, 138–151, https://doi.org/10.3198/1997JoG43-143-138-151, 1997.

Jordan, R. E., Andreas, E. L., and Makshtas, A. P.: Heat budget of snow-covered sea ice at North Pole 4, J. Geophys. Res., 104, 7785–7806, https://doi.org/10.1029/1999JC900011, https://agupubs.onlinelibrary.wiley.com/doi/abs/10.1029/1999JC900011, 1999.

Kaleschke, L., Richter, A., Burrows, J., Afe, O., Heygster, G., Notholt, J., Rankin, A. M., Roscoe, H. K., Hollwedel, J., Wagner, T., and Jacobi, H.-W.: Frost flowers on sea ice as a source of sea salt and their influence on tropospheric halogen chemistry, Geophysical Research Letters, 31, L16 114, https://doi.org/10.1029/2004GL020655, https://agupubs.onlinelibrary.wiley.com/doi/abs/10.1029/2004GL020655, 2004.

Lecomte, O., Fichefet, T., Vancoppenolle, M., and Nicolaus, M.: A new snow thermodynamic scheme for large-scale sea-ice models, Ann. Glaciol., 52, 337–346, 2011.

Ledley, T. S.: Snow on sea ice: Competing effects in shaping climate, J. Geophys. Res., 96, 17 195–17 208, https://doi.org/10.1029/91JD01439, https://agupubs.onlinelibrary.wiley.com/doi/abs/10.1029/91JD01439, 1991.

Lehning, M., Bartelt, P., Brown, B., Russi, T., Stöckli, U., and Zimmerli, M.: SNOWPACK calculations for avalanche warning based upon a new network of weather and snow stations, Cold Reg. Sci. Technol., 30, 145–157, https://doi.org/10.1016/S0165-232X(99)00022-1, 1999.

Lehning, M., Bartelt, P., Brown, B., Fierz, C., and Satyawali, P.: A physical SNOWPACK model for the Swiss avalanche warning Part II: Snow microstructure, Cold Reg. Sci. Technol., 35, 147–167, https://doi.org/10.1016/S0165-232X(02)00073-3, 2002a.

Lehning, M., Bartelt, P., Brown, B., and Fierz, C.: A physical SNOWPACK model for the Swiss avalanche warning Part III: Meteorological forcing, thin layer formation and evaluation, Cold Reg. Sci. Technol., 35, 169–184, https://doi.org/10.1016/S0165-232X(02)00072-1, 2002b.

Leonard, K. C. and Maksym, T.: The importance of wind-blown snow redistribution to snow accumulation on Bellingshausen Sea ice, Ann. Glaciol., 52, 271–278, https://doi.org/10.3189/172756411795931651, 2011.

Lewis, M., Tison, J., Weissling, B., Delille, B., Ackley, S., Brabant, F., and Xie, H.: Sea ice and snow cover characteristics during the winter-spring transition in the Bellingshausen Sea: An overview of SIMBA 2007, Deep-Sea Res. Pt. II, 58, 1019–1038, https://doi.org/10.1016/j.dsr2.2010.10.027, 2011.

Liston, G. E., Polashenski, C., Rösel, A., Itkin, P., King, J., Merkouriadi, I., and Haapala, J.: A Distributed Snow-Evolution Model for Sea-Ice Applications (SnowModel), J. Geophys. Res., 123, 3786–3810, https://doi.org/10.1002/2017JC013706, https://agupubs.onlinelibrary.wiley.com/doi/abs/10.1002/2017JC013706, 2018.

Maksym, T. and Jeffries, M. O.: A one-dimensional percolation model of flooding and snow ice formation on Antarctic sea ice, J. Geophys. Res., 105, 26 313–26 331, https://doi.org/10.1029/2000JC900130, 2000.

Massel, S. R.: Internal Gravity Waves in the Shallow Seas, Springer International Publishing, Switzerland, https://doi.org/10.1007/978-3-319-18908-6, 2015.

Massom, R. A., Drinkwater, M. R., and Haas, C.: Winter snow cover on sea ice in the Weddell Sea, J. Geophys. Res., 102, 1101–1117, https://doi.org/10.1029/96JC02992, https://agupubs.onlinelibrary.wiley.com/doi/abs/10.1029/96JC02992, 1998.

Massom, R. A., Eicken, H., Hass, C., Jeffries, M. O., Drinkwater, M. R., Sturm, M., Worby, A. P., Wu, X., Lytle, V. I., Ushio, S., Morris, K., Reid, P. A., Warren, S. G., and Allison, I.: Snow on Antarctic sea ice, Rev. Geophys., 39, 413–445, https://doi.org/10.1029/2000RG000085, 2001.

Maykut, G. A. and Untersteiner, N.: Some results from a time-dependent thermodynamic model of sea ice, J. Geophys. Res., 76, 1550–1575, https://doi.org/10.1029/JC076i006p01550, https://agupubs.onlinelibrary.wiley.com/doi/abs/10.1029/JC076i006p01550, 1971.

Mualem, Y.: A new model for predicting the hydraulic conductivity of unsaturated porous media, Water Resour. Res., 12, 513–522, https://doi.org/10.1029/WR012i003p00513, 1976.

Nicolaus, M., Haas, C., and Bareiss, J.: Observations of superimposed ice formation at melt-onset on fast ice on Kongsfjorden, Svalbard, Phys. Chem. Earth, 28, 1241–1248, https://doi.org/10.1016/j.pce.2003.08.048, 2003.

Nicolaus, M., Haas, C., Bareiss, J., and Willmes, S.: A model study of differences of snow thinning on Arctic and Antarctic first-year sea ice during spring and summer, Ann. Glaciol., 44, 147–153, https://doi.org/10.3189/172756406781811312, 2006.

Nicolaus, M., Haas, C., and Willmes, S.: Evolution of first-year and second-year snow properties on sea ice in the Weddell Sea during spring-summer transition, J. Geophys. Res., 114, https://doi.org/10.1029/2008JD011227, https://agupubs.onlinelibrary.wiley.com/doi/abs/10.1029/2008JD011227, 2009.

Notz, D.: Challenges in simulating sea ice in Earth System Models, WIREs Clim. Change, 3, 509–526, https://doi.org/10.1002/wcc.189, https://onlinelibrary.wiley.com/doi/abs/10.1002/wcc.189, 2012.

Obleitner, F. and Lehning, M.: Measurement and simulation of snow and superimposed ice at the Kongsvegen glacier, Svalbard (Spitzbergen), J. Geophys. Res., 109, https://doi.org/10.1029/2003JD003945, https://agupubs.onlinelibrary.wiley.com/doi/abs/10.1029/2003JD003945, 2004.

Perovich, D., Jones, K., Light, B., Eicken, H., Markus, T., Stroeve, J., and Lindsay, R.: Solar partitioning in a changing Arctic sea-ice cover, Ann. Glaciol., 52, 192–196, https://doi.org/10.3189/172756411795931543, 2011.

Petty, A. A., Webster, M., Boisvert, L., and Markus, T.: The NASA Eulerian Snow on Sea Ice Model (NESOSIM) v1.0: initial model development and analysis, Geosci. Model Dev., 11, 4577–4602, https://doi.org/10.5194/gmd-11-4577-2018, https://www.geosci-model-dev.net/11/4577/2018/, 2018.

Picard, G., Sandells, M., and Löwe, H.: SMRT: an active–passive microwave radiative transfer model for snow with multiple microstructure and scattering formulations (v1.0), Geosci. Model Dev., 11, 2763–2788, https://doi.org/10.5194/gmd-11-2763-2018, https://www.geosci-model-dev.net/11/2763/2018/, 2018.

Poisson, A. and Papaud, A.: Diffusion coefficients of major ions in seawater, Mar. Chem., 13, 265–280, https://doi.org/10.1016/0304-4203(83)90002-6, 1983.

Rankin, A. M., Wolff, E. W., and Martin, S.: Frost flowers: Implications for tropospheric chemistry and ice core interpretation, J. Geophys. Res., 107, https://doi.org/10.1029/2002JD002492, https://agupubs.onlinelibrary.wiley.com/doi/abs/10.1029/2002JD002492, 2002.

Steger, C. R., Reijmer, C. H., van den Broeke, M. R., Wever, N., Forster, R. R., Koenig, L. S., Kuipers Munneke, P., Lehning, M., Lhermitte, S., Ligtenberg, S. R. M., Miège, C., and Noël, B. P. Y.: Firn Meltwater Retention on the Greenland Ice Sheet: A Model Comparison, Front. Earth Sci., 5, 3, https://doi.org/10.3389/feart.2017.00003, https://www.frontiersin.org/article/10.3389/feart.2017.00003, 2017.

Sturm, M., Perovich, D. K., and Holmgren, J.: Thermal conductivity and heat transfer through the snow on the ice of the Beaufort Sea, J. Geophys. Res., 107, SHE 19–1–SHE 19–17, https://doi.org/10.1029/2000JC000409, https://agupubs.onlinelibrary.wiley.com/doi/abs/10.1029/2000JC000409, 2002.

Toyota, T., Takatsuji, S., Tateyama, K., Naoki, K., and Ohshima, K. I.: Properties of sea ice and overlying snow in the Southern Sea of Okhotsk, J. Oceanogr., 63, 393–411, https://doi.org/10.1007/s10872-007-0037-2, https://doi.org/10.1007/s10872-007-0037-2, 2007.

Tremblay, L.-B. and Mysak, L. A.: Modeling Sea Ice as a Granular Material, Including the Dilatancy Effect, J. Phys. Oceanogr., 27, 2342–2360, https://doi.org/10.1175/1520-0485(1997)027<2342:MSIAAG>2.0.CO;2, 1997.

Trujillo, E., Leonard, K., Maksym, T., and Lehning, M.: Changes in snow distribution and surface topography following a snowstorm on Antarctic sea ice, J. Geophys. Res., 121, 2172–2191, https://doi.org/10.1002/2016JF003893, https://agupubs.onlinelibrary.wiley.com/doi/abs/10.1002/2016JF003893, 2016.

Turner, A. K. and Hunke, E. C.: Impacts of a mushy-layer thermodynamic approach in global sea-ice simulations using the CICE sea-ice model, J. Geophys. Res., 120, 1253–1275, https://doi.org/10.1002/2014JC010358, https://agupubs.onlinelibrary.wiley.com/doi/abs/10.1002/2014JC010358, 2014.

Ukita, J. and Martinson, D. G.: An efficient adjustable-layering thermodynamic sea-ice model formulation for high-frequency forcing, Ann. Glaciol., 33, 253–260, https://doi.org/10.3189/172756401781818194, 2001.

van Genuchten, M. T.: A Closed-form Equation for Predicting the Hydraulic Conductivity of Unsaturated Soils, Soil Sci. Soc. Am. J., 44, 892–898, https://doi.org/10.2136/sssaj1980.03615995004400050002x, 1980.

Vancoppenolle, M., Goosse, H., de Montety, A., Fichefet, T., Tremblay, B., and Tison, J.-L.: Modeling brine and nutrient dynamics in Antarctic sea ice: The case of dissolved silica, J. Geophys. Res., 115, https://doi.org/10.1029/2009JC005369, https://agupubs.onlinelibrary.wiley.com/doi/abs/10.1029/2009JC005369, 2010.

Veldman, A. E. P. and Rinzema, K.: Playing with nonuniform grids, Journal of Engineering Mathematics, 26, 119–130, https://doi.org/10.1007/BF00043231, https://doi.org/10.1007/BF00043231, 1992.

Weiss, A. I., King, J., Lachlan-Cope, T., and Ladkin, R.: On the effective aerodynamic and scalar roughness length of Weddell Sea ice, J. Geophys/ Res., 116, D19 119, https://doi.org/10.1029/2011JD015949, https://agupubs.onlinelibrary.wiley.com/doi/abs/10.1029/2011JD015949, 2011.

Wever, N., Fierz, C., Mitterer, C., Hirashima, H., and Lehning, M.: Solving Richards Equation for snow improves snowpack meltwater runoff estimations in detailed multi-layer snowpack model, Cryosphere, 8, 257–274, https://doi.org/10.5194/tc-8-257-2014, 2014.

Wever, N., Schmid, L., Heilig, A., Eisen, O., Fierz, C., and Lehning, M.: Verification of the multi-layer SNOWPACK model with different water transport schemes, Cryosphere, 9, 2271–2293, https://doi.org/10.5194/tc-9-2271-2015, http://www.the-cryosphere.net/9/2271/2015/, 2015.

Wever, N., Würzer, S., Fierz, C., and Lehning, M.: Simulating ice layer formation under the presence of preferential flow in layered snowpacks, Cryosphere, 10, 2731–2744, https://doi.org/10.5194/tc-10-2731-2016, http://www.the-cryosphere.net/10/2731/2016/, 2016.

Yamaguchi, S., Watanabe, K., Katsushima, T., Sato, A., and Kumakura, T.: Dependence of the water retention curve of snow on snow characteristics, Ann. Glaciol., 53, 6–12, https://doi.org/10.3189/2012AoG61A001, 2012.